

# Multi-scale rupture growth with alternating directions in a complex fault network during the 2023 south-eastern Türkiye and Syria earthquake doublet

Ryo Okuwaki<sup>1</sup>, Yuji Yagi<sup>1</sup>, Tuncay Taymaz<sup>2</sup>, Stephen P. Hicks<sup>3</sup>

<sup>1</sup>Faculty of Life and Environmental Sciences, University of Tsukuba, Tsukuba, Ibaraki 305-8572, Japan

<sup>2</sup>Department of Geophysical Engineering, The Faculty of Mines, Istanbul Technical University, Maslak, 34469 Sariyer, Istanbul, Türkiye

<sup>3</sup>Department of Earth Sciences, University College London, Gower Street, London, WC1E 6BT, UK

## Key Points:

- An earthquake doublet of  $M_W$  7.9 and  $M_W$  7.6 ruptured multiple segments and curved faults
- Initial splay fault rupture triggered a large  $M_W$  7.9 rupture involving pulses of back-propagating supershear rupture
- Multi-scale rupture growth in a complex fault network may facilitate diverse rupture behaviors and triggering interactions in the doublet

## Abstract

A devastating doublet of earthquakes with moment magnitude  $M_W$  7.9 and  $M_W$  7.6 earthquakes contiguously occurred in SE Türkiye near the NW border of Syria. Here we perform a potency-density tensor inversion to simultaneously estimate rupture evolution and fault geometry for the doublet. We find the initial  $M_W$  7.9 earthquake involved discrete episodes of supershear rupture and back-rupture propagation, and was triggered by initial rupture along a bifurcated splay of the East Anatolian Fault. The second  $M_W$  7.6 event was triggered by the earlier  $M_W$  7.9 event, and it involved more extensive supershear rupture along a favorably curved fault, and was likely stopped by geometric barriers at the fault ends. Our results highlight the multi-scale cascading rupture growth across the complex fault network that affects the diverse rupture geometries of the 2023 Türkiye earthquake doublet, contributing to the strong ground shaking and associated devastation.

## Plain Language Summary

On 6 February 2023, devastating dual earthquakes; moment magnitude 7.9 and 7.6 events struck southern Türkiye near the northern border of Syria. The two earthquakes were only separated ~90 km and ~9 hours apart. The strong shaking from the two earthquakes

---

Corresponding author: Ryo Okuwaki, [rokuwaki@geol.tsukuba.ac.jp](mailto:rokuwaki@geol.tsukuba.ac.jp)

caused significant damage to the buildings and people, having caused over 50,000 fatalities in Türkiye and Syria. The source region is where the Anatolian, Arabian and African plates meet, developing the network of faults that hosted the large devastating earthquakes. Seismological analyses using observed seismic waveforms are effective for rapidly estimating how the rupture of the two earthquakes evolves over such distinctively oriented and possibly segmented faults. We use the globally observed seismic records to simultaneously estimate rupture evolution and fault geometry of the earthquake doublet. We find the sequence of both earthquakes involves curved and segmented fault ruptures, including the back-propagating rupture for the initial earthquake, which is facilitated by the complex active fault network. The 2023 earthquake doublet displays the irregular rupture evolution and diverse triggering behaviors both in a single event and across the earthquake sequence, which provide critical inputs in both our understanding of earthquake-rupture dynamics and better assessment of future damaging earthquakes.

## 1 Introduction

The Eastern Mediterranean region is one of Earth's most active tectonic environments, where the Anatolian plate is extruded westward, escaping from the collision between the Arabian and Eurasian plates (McKenzie, 1972; Taymaz, Jackson, & McKenzie, 1991; Taymaz, Eyidogan, & Jackson, 1991; Taymaz et al., 2004). To the southeast of the Anatolian plate, the left-lateral East Anatolian Fault (EAF), along with the right-lateral North Anatolian Fault (NAF), accommodates the extrusion of the Anatolian plate (Jackson & McKenzie, 1984; Taymaz, Eyidogan, & Jackson, 1991; Taymaz et al., 2021). The EAF forms an intra-continental transform fault, which separates the Anatolian and Arabian plates (Fig. 1). Although the EAF has been less seismically active than that around the NAF since instrumental-based catalogues started (e.g., Ambraseys, 1989), the EAF has hosted magnitude  $M$  7+ earthquakes in the past, for example, an  $M$  7.1 1893 in Çelikhhan, an  $M$  7.4 1513 in Pazarcık, and an  $M$  7.5 in 1822 to the east of Hassa (Ambraseys, 1989; Ambraseys & Jackson, 1998; Duman & Emre, 2013). Most recently, in 2020, a moment magnitude  $M_W$  6.8 Doğanyol–Sivrice earthquake broke the region east of the 1893  $M$  7.1 earthquake (Melgar et al., 2020; Pousse-Beltran et al., 2020; Ragon et al., 2021; Taymaz et al., 2021), located to the north-east of the 2023 earthquakes focused on in this study. The EAF is recognized to have multiple geometrically segmented faults and a series of bends, step-overs, and sub-parallel faults, leading to complex fault networks (Fig. 1) (e.g., Duman & Emre, 2013). This complexity is particularly evident in southern Türkiye, where the EAF connects to the triple junction of the Anatolian, Arabian and African plates, and the main plate boundary merges into the Dead Sea Fault (DSF) zone to the south. This diffuse zone of deformation manifests as a rotation in the strike of the main EAF from NE-SW in the NE to SSW-NNE near the town of Pazarcık, SW Kahramanmaraş province (Fig. 1). To the north of Kahramanmaraş province, the EW-oriented Sürgü fault zone (SFZ), obliquely branches from the main EAF (Arpat & Saroglu, 1972; Taymaz, Eyidogan, & Jackson, 1991; Duman & Emre, 2013; Duman et al., 2020).

Two devastating earthquakes with  $M$  7.7 and  $M$  7.6 (AFAD, 2023) occurred on February 6, 2023 near the SW end of the EAF in Nurdağı-Pazarcık segment, SE Türkiye near the northern border of Syria (AFAD, 2023; Melgar et al., 2023; Barbot et al., 2023; Rosakis

77 et al., 2023; Zahradník et al., 2023; Delouis et al., 2023). In the following, we refer to  
78 the magnitude of those earthquakes as  $M_W$  7.9 and  $M_W$  7.6, respectively, based on our  
79 own estimates that will be presented in the following sections. The two earthquakes oc-  
80 curred only  $\sim 9$  hours and  $\sim 90$  km apart (Fig. 1). The epicenters reported by AFAD (2023)  
81 show that the initial  $M_W$  7.9 earthquake seems to have initiated off the main EAF strand  
82 in the Narlıdağ fault zone (Duman & Emre, 2013), lying  $\sim 15$  km to the east (Fig. 1). In  
83 contrast, the secondary  $M_W$  7.6 earthquake lies near the SFZ (Fig. 1). The relocated af-  
84 tershocks (Melgar et al., 2023) seemingly align with the main EAF strand and the north-  
85 ern strand of the EAF, whilst some other linear trends and clusters can be seen off the  
86 main EAF segment. For example, around the epicenter of the initial  $M_W$  7.9 earthquake,  
87 some aftershocks appear to branch away from the main EAF (Fig. 1). Global Centroid  
88 Moment Tensor (GCMT) solutions (Dziewonski et al., 1981; Ekström et al., 2012) for the  
89 two earthquakes have oblique left-lateral strike-slip faulting. The fault orientations of  
90 the two solutions are apparently consistent with the bulk orientations of the main EAF  
91 segment and the SFZ respectively (Fig. 1), however, the moment tensors show moderately-  
92 high non-double couple components of 42% and 57%.

93 The geometric complexity of the EAF and the adjacent fault networks, the appar-  
94 ent offset of the initial  $M_W$  7.9 epicenter from the main EAF strand, the high non-double  
95 couple components of the GCMT solutions, and the aftershock distribution with diverse  
96 orientations collectively suggest the earthquake sequence involved complexity in both  
97 rupture evolution and fault geometry (Abercrombie et al., 2003; Okuwaki et al., 2021;  
98 Okuwaki & Fan, 2022). In general, geometric complexities of a fault system are known  
99 to control rupture speed and direction, and triggering of separated fault segments (Das  
100 & Aki, 1977; Kase & Day, 2006; Yıkılmaz et al., 2015; Huang, 2018). There is also grow-  
101 ing observational evidence of rupture irregularity within fault damage zones in differ-  
102 ent tectonic regimes, such as transient supershear ruptures across fault bends (Bao et  
103 al., 2019; Socquet et al., 2019), triggering of ruptures with different faulting styles and  
104 on different segments (Wei et al., 2011; Nissen et al., 2016; Ruppert et al., 2018), and ap-  
105 parent rupture back-propagation or re-rupture (Hicks et al., 2020; Gallovič et al., 2020;  
106 Yamashita, Yagi, & Okuwaki, 2022; Yagi et al., 2023). Such diverse rupture behavior in  
107 different tectonic environments and fault zones gives fundamental inputs that deepen  
108 and accelerate our understanding of earthquake-source physics and the knock-on ef-  
109 fects on strong ground motion. However, it has been challenging for seismologists to  
110 rigorously retrieve rupture complexity that should be recorded in rich waveform datasets,  
111 because of the necessity of assumptions involving the fault geometry and rupture di-  
112 rection, which are often not necessarily required by the data itself and sometimes bias  
113 the interpretation of the earthquake source process. The methodological difficulties in  
114 analyzing geometrically complex earthquakes are a huge obstacle in our understand-  
115 ing of earthquake source physics, but also hinder rapid and robust response, especially  
116 for destructive events like the 2023 SE Türkiye and Syria earthquake sequence, and as-  
117 sessing of future earthquake (e.g., aftershock) hazard in the short-to-medium term (e.g.,  
118 Dal Zilio & Ampuero, 2023; Hussain et al., 2023; Hall, 2023).

119 Here we report a narrative of rupture evolution of the two  $M_W$  7.9 and  $M_W$  7.6 earth-  
120 quakes using teleseismic  $P$ -waveforms observed globally at broadband seismic stations.  
121 We find the two nearby earthquakes ruptured multiple segments and branches of the

122 EAF, and involving curved faults, which likely influenced slip acceleration and decel-  
123 eration during discrete rupture episodes. Most notably, the initial  $M_W$  7.9 earthquake  
124 involved an apparent back-propagating supershear rupture through and beyond the hypocen-  
125 ter area, which should be responsible for the series of triggering of sub-events in their  
126 unfortunately favorable orientation.

## 127 2 Materials and Methods

128 In general, finite fault inversion estimates the spatio-temporal slip distribution on  
129 an assumed fault plane (Olson & Apsel, 1982; Hartzell & Heaton, 1983). Such modeled  
130 fault geometries may be refined using field observations and satellite imagery that cap-  
131 tures the surface deformation. However, strictly prescribing fault geometry may bias  
132 our interpretation of the solution, because limiting model flexibility can mask subtle  
133 rupture details and fault geometries beyond what can sometimes be observed at the sur-  
134 face (e.g., Shimizu et al., 2020). Similar problems may arise when strict assumptions are  
135 made about kinematic information such as rupture velocity and direction.

136 In this study, we perform a recently developed potency-density tensor inversion  
137 (Shimizu et al., 2020; Yamashita, Yagi, Okuwaki, Shimizu, et al., 2022) for both the  $M_W$  7.9  
138 and  $M_W$  7.6 earthquakes using teleseismic  $P$ -waves. Our approach is particularly effec-  
139 tive for analyzing complex earthquake sequences, because it does not require any de-  
140 tailed assumptions about the fault geometry, but rather, we simultaneously solve for fault  
141 geometry and slip as data requires. In this study, we configured the model-space geom-  
142 etry based on the recognized active faults (Emre et al., 2018) and the relocated aftershocks  
143 (Melgar et al., 2023) around the source region of the two earthquakes (Fig. S3). Regard-  
144 less of this model-space parameterization, one strength of our approach is that the po-  
145 tency tensors at each source element remain flexible to represent fault geometry that  
146 deviates from the prescribed model-fault geometry. This modeling flexibility is partic-  
147 ularly advantageous for analyzing an earthquake in a complex fault zone, where there  
148 are multiple segments of faults with different orientations, and possible supershear rup-  
149 tures, which are likely factors for the 2023 SE Türkiye earthquake doublet given the strike-  
150 slip configuration and known structure of the EAF.

151 We adopted a maximum rupture-front speed of 4 km/s based on the upper limit  
152 of  $S$ -wave velocity near the source (Table S1) so that the model space can capture pos-  
153 sible supershear rupture or inter-subevent dynamic triggering. We also tested a faster  
154 maximum rupture-front speed at 5 km/s, and the key features of the rupture process  
155 that we discuss next were reproduced (Fig. S11). We also adopted a sufficiently long max-  
156 imum slip duration at each source element of 42 s and a total source duration of 80 s  
157 for the initial earthquake and a maximum slip duration at each source element of 20 s  
158 and a total source duration of 20 s for the second earthquake (Fig. 2). We represent potency-  
159 rate functions as a set of linear B splines (multi-time window), and we adopted suffi-  
160 ciently long durations so that each source element can flexibly represent possible mul-  
161 tiple slip episodes as data requires. As we will present later, our key finding of appar-  
162 ent back-rupture propagation is robustly resolved against the different assumptions of  
163 maximum slip duration at each source element (Fig. S10).

164 Our modeling strategy shares a similarity with that of seismic back-projection, which  
165 requires very few assumptions about the fault geometry and rupture information (Ishii  
166 et al., 2005; Y. Xu et al., 2009; Meng et al., 2012; Nissen et al., 2016; Satriano et al., 2012;  
167 Yao et al., 2011; Taymaz et al., 2021). Our approach additionally provides kinematic in-  
168 formation by directly solving for the potency-rate density distribution, which should  
169 enable in-depth evaluation of rupture dynamics that, for example, can be associated with  
170 variable fault geometry. To perform a stable inversion with such a high degree-of-freedom  
171 model without overfitting, the uncertainty of the Green's function is incorporated into  
172 the data covariance matrix (Yagi & Fukahata, 2011) and the strength of smoothing is ad-  
173 justed using the Akaike's Bayesian Information Criterion (e.g., Akaike, 1980; Yabuki &  
174 Matsu'ura, 1992; Sato et al., 2022). We note the effect of structural heterogeneity can  
175 also be translated into the uncertainty of Green's functions if it is stochastic, yet it still  
176 impacts the finite-fault solution given the complex tectonic setting in the study region,  
177 which may affect the relative timing of rupture. As demonstrated in Fig. S9, allowing  
178 a high degree of freedom of modeling should rather help stabilize the solution; for ex-  
179 ample, only allowing pure vertical strike-slip faulting yields poor data fits (Fig. S9) and  
180 an unstable solution that yields an opposite sense-of-slip to what is expected for the re-  
181 gional tectonic regime (e.g., Fukahata & Wright, 2008). This exercise highlights the im-  
182 portance of permitting a complex rupture scenario with enough model freedom and over-  
183 constraining the model would fail to explain the seismic signals that are responsible for  
184 the change of focal mechanism during rupture (e.g., Shimizu et al., 2020). Aftershock  
185 focal mechanisms and moment tensors show a variability with a deviation from pure  
186 strike-slip faulting (Fig. 1), helping to demonstrate that a flexible potency-density ten-  
187 sor approach is required.

188 We applied a standardized data processing workflow for our potency-density ten-  
189 sor approach that has been applied to earthquakes in different tectonic regimes (Shimizu  
190 et al., 2020; Tadapansawut et al., 2021; Hu et al., 2021; Fan et al., 2022; Fang et al., 2022;  
191 Hicks et al., 2020; Yamashita, Yagi, Okuwaki, Shimizu, et al., 2022; Yagi et al., 2023). We  
192 used the vertical component of teleseismic  $P$ -waveforms from a total of 39 and 37 sta-  
193 tions for the  $M_W$  7.9 and  $M_W$  7.6 earthquakes, respectively (Figs. S1 and S2). The data  
194 were selected to ensure sufficient azimuthal coverage so that we can resolve potential  
195 variations of radiation pattern during the rupture evolution and hence spatiotemporal  
196 changes of fault geometry. We selected data so that we manually picked the first mo-  
197 tion of  $P$ -wave (e.g., Okuwaki et al., 2016). The data were then restituted to velocity at  
198 1.0-s sampling interval by removing the instrumental responses. Green's functions were  
199 calculated based on the method of Kikuchi and Kanamori (1991), adopting CRUST1.0  
200 model (Laske et al., 2013) for the one-dimensional layered velocity structure around the  
201 source region (Table S1). We further tested the robustness of our modeling against an  
202 alternative structural model adopted from the ak135 model (Kennett et al., 1995) (Ta-  
203 ble S2), showing that the resultant pattern of potency-density tensors is less sensitive  
204 to the choice of the near-source structure model (Fig. S7). The initial rupture point is  
205 taken from the relocated epicenter for the  $M_W$  7.9 earthquake (Melgar et al., 2023) and  
206 on the model fault near the relocated epicenter for the  $M_W$  7.6 earthquake. We set the  
207 hypocentral depth at 15 km for both earthquakes (Fig. S3). The uniformly-distributed  
208 model source elements are regularly spaced  $10 \times 5$  km and  $5 \times 5$  km in the along-strike  
209 and dip directions for the  $M_W$  7.9 and  $M_W$  7.6 earthquakes, respectively, along a ver-

210 tically dipping non-planar model fault that aligns with the active faults (Emre et al., 2018)  
211 and the relocated aftershocks (Fig. S3). Together with the curved main EAF strand, we  
212 adopted a splay fault into our model fault centered on the initial rupture point, which  
213 is oriented at 35° NE, having an acute angle relative to the main EAF in NE direction  
214 (Fig. S3).

### 215 3 Results

#### 216 3.1 Initial $M_W$ 7.9 Nurdağı-Pazarcık earthquake

217 Our potency-density tensor inversion finds the first earthquake ruptured a total  
218 of 350 km length; 200 km length northeast from the epicenter and 150 km southwest  
219 of the epicenter along our modeled fault, including the splay fault domain (Figs. 2 and  
220 S4). The total seismic moment is  $9.6 \times 10^{20}$  N m ( $M_W$  7.9), which is similar to the that  
221 estimated from coda waves (X. Jiang et al., 2023). The overall faulting mechanism in-  
222 dicated by the flexible potency density tensors is consistent with our prescribed non-  
223 planar model fault geometry (Fig. 2). The potency-density tensors show a largely pla-  
224 nular fault with depth. The space-time evolution of the rupture shows four distinct episodes  
225 which we describe in the following paragraphs.

226 **Rupture Episode 1.** The first-motion faulting mechanism using local-regional wave-  
227 forms (Fig. 3) indicates this rupture initiated at the hypocentre along a fault plane with  
228 a NW-SE fault, but with an oblique-normal sense of slip after nucleation, the rupture  
229 then propagates bilaterally toward the NE and SW for the first 10 s after origin time (OT),  
230 extending 25 km either side of the hypocenter along the splay fault. The moment-rate  
231 release of this initial rupture episode is minor, having only 3% of the total seismic moment  
232 ( $M_W$  6.9). Our potency-rate density tensor solution shows left-lateral faulting on  
233 a faulting striking 36° (based on the largest potency rate in 7–8 s time window; Fig. 3),  
234 more consistent with the prescribed splay fault rather than the main EAF (Fig. 3).

235 **Rupture Episode 2.** After a relative quiescence for 5 s after the end of the first episode,  
236 the second rupture episode starts at OT+15 s, lying 60 km NE of the epicenter. This episode  
237 releases the greatest amount of seismic moment (35%;  $M_W$  7.6) of the entire rupture.  
238 The rupture propagates in an asymmetric bilateral manner with a strong SW-oriented  
239 direction, rupturing a total length of 120 km over 20 s duration. Most notably, the SW  
240 flank of the rupture front apparently back-propagates through the hypocentral region  
241 beyond 20 km SW of the epicenter (Fig. 2). The migration speed of the associated SW-  
242 directing back-propagating rupture signal exceeds the local S-wave velocity (Table S1;  
243 Laske et al., 2013) (Fig. 2; Movies S1 and S2), indicating super-shear rupture during the  
244 latter portion of this rupture episode. Although rigorous estimates of rupture velocity  
245 can be limited due to the smoothing constraints, the migration speed of this high slip-  
246 rate zone is related to the rupture-front velocity (Okuwaki et al., 2020), and has been  
247 calibrated well with rupture velocities from independent back-projection results for other  
248 earthquakes (e.g., Hicks et al., 2020). The fault geometry estimated from our potency-  
249 density tensor approach shows vertical strike-slip faulting with a strike of 55° (e.g., where  
250 we solved the largest potency rate at 22–23 s; Fig. 3) that is consistent with the main EAF.  
251 We note that the source elements with minor potency rate may be affected by the sur-

252 rounding major potency rate due to smoothing effects, so we do not interpret the resul-  
253 tant strike angle from those minor potency-rate tensors.

254 **Rupture Episode 3.** A third rupture phase NE of the hypocentre begins to be dom-  
255 inant from OT+35 s, soon after the SW back-rupture propagation decays. This phase  
256 accounts for 15% of the total seismic moment ( $M_W$  7.4). It first propagates to the SW  
257 near the NE flank of the second rupture episode, but then the NE-oriented component  
258 of the bilateral rupture becomes more dominant during OT+37–45 s, rupturing a to-  
259 tal length of 100 km until it immediately stops near the NE edge of the model domain  
260 at 120 km NE from the epicenter (Fig. 2). The strike orientation is similar to that of Episode  
261 2 and remains consistent with the main EAF. We refrain from measuring rupture speeds  
262 for this episode as they seem sensitive to the assumption of maximum slip duration (Fig.  
263 S10).

264 **Rupture Episode 4.** A fourth rupture episode starts at OT+45 s in the SW corner  
265 of the model domain, partially overlapping in space with the second rupture. The rup-  
266 ture front unilaterally propagates toward the SW at fast, supershear speed, exceeding  
267 the local *S*-wave velocity during OT+45–55 s. Then, the rupture front apparently slows  
268 down ~150 km SW of the junction between the EAF and splay faults, and completely  
269 stops at 75 s. The strike orientation is 54° (based on the largest potency rate in 50–51 s  
270 time window). The fourth rupture episode has 43% of the total seismic moment ( $M_W$  7.7),  
271 and the potency-density tensors have a median non-double couple component of 24%  
272 (e.g., 60–61 s; Fig. 3).

### 273 3.2 Secondary $M_W$ 7.6 Ekinözü earthquake

274 The rupture of the later  $M_W$  7.6 earthquake is much more confined, rupturing 80  
275 km length and 20 km width over a single episode, and the total seismic moment is  $3.2 \times$   
276  $10^{20}$  N m ( $M_W$  7.6). The rupture evolution is asymmetric bilateral with a dominant westwards-  
277 directed rupture from the epicenter. The west-oriented rupture propagates at faster than  
278 the local *S*-wave velocity (Table S1; Fig. 2; Movies S1 and S3) from 6 to 10 s. The rup-  
279 ture immediately stops at around 15 s. The fault geometry estimated from our potency-  
280 density tensors has an EW-oriented curved fault strike with strike-slip faulting, which  
281 is well aligned with the prescribed curved model plane geometry. The estimated fault  
282 dip is dominantly vertical, but the dip angle slightly shallows with depth from 76° to  
283 61°, as defined by the maximum along-strike potency density (Fig. S4b). Near the end  
284 of the rupture, dip-slip faulting components become dominant at the tips of the main  
285 rupture, with strikes rotated north-south (Fig. 3).

## 286 4 Discussion

### 287 4.1 $M_W$ 7.9 event: rupture initiation on a splay fault to the main EAF

288 The initial rupture of the  $M_W$  7.9 event has a different fault orientation than that  
289 of the following main bilateral rupture that releases most (97%) of the seismic moment.  
290 For example, during the peak slip of the first rupture episode (7–8 s), the strike is 36°,  
291 whilst the later bilateral rupture episode has a strike of 55° (Fig. 3). Intense aftershock  
292 activity is observed NE of the epicenter (Melgar et al., 2023), in a lineation oriented SW

293 to NE, seemingly connecting to the main EAF strand (Fig. 3). The alignment of these af-  
294 tershocks on the splay fault is consistent with the strike estimated from our inversion.  
295 To the east of the epicenter, the Narlıdağ fault zone has been mapped to extend to the  
296 N and NE (Perinçek & Çemen, 1990; Duman & Emre, 2013). From rapid analyses of the  
297 satellite images and field measurements, surface rupture is also observed near the epi-  
298 center, which is elongated NE and is consistent with our estimated strike orientation (Reitman  
299 et al., 2023), which is called as Nurdağı-Pazarcık fault by Melgar et al. (2023). Thus, the  
300 first rupture episode occurred on a sub-parallel splay fault to the main EAF. Although  
301 our potency-density tensor inversion finds mostly pure strike-slip faulting during the  
302 first rupture episode, the first-motion mechanism from near-field waveforms suggest  
303 that the rupture initiated with a weak phase of oblique-normal faulting (Fig. 3c), which  
304 is likely too small to be resolved in teleseismic waveforms. From our estimated strike  
305 orientations, the angle between the splay fault and the main EAF model domain is  $\sim 18^\circ$ ,  
306 which is close to the peak of the splay fault angle distributions ( $\pm 17^\circ$ ) that was previ-  
307 ously observed for active faults in California (Ando et al., 2009; Scholz et al., 2010). In  
308 between the first and second rupture episodes, we only see minor moment release, which  
309 may suggest a non-continuous rupture at the junction between the splay fault and main  
310 EAF. However, due to the insufficient spatial resolution of the teleseismic data we used,  
311 it is difficult to rigorously discuss how the splay fault and the main EAF are physically  
312 connected solely based on our result.

#### 313 **4.2 Rupture dynamics during apparent back-propagating slip**

314 One of the most notable features of the  $M_W$  7.9 earthquake is the asymmetric bi-  
315 lateral rupture of the second episode during OT+15–35 s (Fig. 2), where the SW flank  
316 of the bilateral rupture apparently propagates back through the hypocentral area. We  
317 confirmed this apparent back-propagation rupture behavior is robustly retrieved even  
318 if we changed model assumptions, such as the maximum duration of bases slip func-  
319 tions and the hypothesized rupture-front speed (Figs. S10 and S11). Such a boomerang-  
320 like back rupture propagation is an end-member rupture behavior that has become more  
321 frequently reported with higher-resolution datasets and more detailed rupture imag-  
322 ing (Meng et al., 2018; Hicks et al., 2020; Yamashita, Yagi, & Okuwaki, 2022; Vallée et  
323 al., 2023). However, because the earthquakes in all of these cases studied were either  
324 deep or in remote areas, there were no surface rupture observations that could have ex-  
325 plained the apparent back-rupture propagation. Therefore, the apparent boomerang rup-  
326 ture of the 2023 SE Türkiye earthquake is intriguing because we show that the rupture  
327 propagated along different sub-parallel fault strands which could offer an mechanism  
328 for these previously reported examples of back-propagating ruptures.

329 Although it is still difficult to find a deterministic explanation of why the initial  
330 rupture occurred on the more minor bifurcated fault rather than the main EAF, the se-  
331 ries of multiple ruptures that are responsible for the resultant boomerang-like rupture  
332 can be explained by a cascading up of rupture size based on a hierarchical rupture model  
333 (e.g., Ide & Aochi, 2005; Otsuki & Dilov, 2005). In this case, the main rupture could have  
334 been dynamically triggered by the initial splay fault rupture as it cascades up to the longer  
335 scale of the rupture. The main EAF should have accumulated enough strain due to the  
336 plate accommodation (e.g., Aktug et al., 2016; Weiss et al., 2020), which makes it ready



337 to be ruptured once assisted by the initial rupture on the bifurcated fault. Although our  
338 sole use of teleseismic data may not rigorously discriminate the absolute location of the  
339 slip on the closely located parallel faults, we favor that the apparent back-propagating  
340 part of the rupture occurred on the main EAF because of the higher potency rate on the  
341 main EAF model fault rather than on the splay model fault (Fig. 2c,d). This assumption  
342 is supported by independent modeling using geodetic datasets that finds larger slip along  
343 the main EAF than on the splay fault (Barbot et al., 2023; Mai et al., 2023; Melgar et al.,  
344 2023).

345 Rupture dynamics across branching faults have been extensively studied by nu-  
346 merical simulations (Kame et al., 2003; Ando & Yamashita, 2007; Aochi et al., 2000; Bhat  
347 et al., 2007; S. Xu et al., 2015; Okubo et al., 2020). Backward branching rupture is par-  
348 ticularly proposed (Fliss et al., 2005), where stress accumulation at the tip of the main  
349 fault enhances rupture jump onto the neighboring branch fault, nucleating bilateral rup-  
350 ture in which one flank can be seen as apparent backward rupture. Although it remains  
351 to be solved whether the initial rupture is physically intersecting the main EAF or not,  
352 our source model shows that the initial rupture is not continuously propagating with  
353 a sufficiently strong slip-rate into the main EAF, and the second rupture episode begins  
354 on the main EAF ~20 km SW from the apparent junction of the initial fault strand and  
355 the main EAF. The spatiotemporal gap between the initial and second rupture episodes  
356 might play a role to enable the cascade up or jump of rupture to the larger scale main  
357 rupture. The main EAF west of the junction with the Narlıdağ fault zone should be situ-  
358 ated in the extensional quadrant of the left-lateral Rupture Episode 1, which may im-  
359 part a stress shadow on the main EAF. Such a stress shadow may have disrupted the SW-  
360 directed Rupture Episode 2, which we see as a temporary rupture deceleration at OT+15–  
361 20 s before it then accelerated to a discrete phase of supershear rupture (Fig. 2). The rup-  
362 ture propagation toward SW through the hypocentral region may be enabled because  
363 the longer-scale main EAF rupture should have enough fracture energy to easily over-  
364 come the area affected by the stress shadow possibly generated by the lower level of rup-  
365 ture episode. Dynamic rupture simulations will help to shed further light on rupture  
366 processes across this fault junction (e.g., Rosakis et al., 2023).

367 The strike orientation during the second rupture episode (OT+15–20 s) is slightly  
368 rotated clockwise, which is also mapped in the main EAF strand west of the junction  
369 (Figs. 1 and 3). If this change in fault orientation acts as a restraining bend given the back-  
370 ground stress field, the rupture propagation may cause a concentration of stress at the  
371 bend. This might have caused the rupture deceleration, which can be seen as the slip  
372 stagnation during OT+15–20 s. Soon after this pause, dynamic stresses allowed the rup-  
373 ture to continue and propagate to the SW and even briefly accelerate its speed, which  
374 can be consistent with the predicted behavior of a supershear rupture transition across  
375 restraining bends (e.g., Bruhat et al., 2016). We emphasize here that our source model  
376 does show that the Mw 7.9 earthquake is not supershear throughout the entire event,  
377 but it involves discrete supershear along certain fault segments during each rupture episode.  
378 Such discrete supershear pulses have been independently estimated using near-field records  
379 (e.g., Delouis et al., 2023) and numerical simulations (e.g., Abdelmeguid et al., 2023).

380 We further note that the NE and SW boundaries of the second rupture episode co-  
381 incide with mapped fault steps near Gölbaşı and south of Nurdağı (see locations S1 and

382 S2 in Fig. S5). Such steps may contribute to the apparent gaps of 10 s between the sec-  
383 ond and subsequent rupture episodes (Fig. S5). We do not have enough evidence to ex-  
384 plain how such gaps are physically connected, but our finding will stimulate further re-  
385 search to investigate how the rupture evolved across fault steps, for example, the long  
386 nucleation processes or possibly inter-subevent slow deformation.

### 387 4.3 The SW-end third rupture episode broke multiple fault segments

388 Together with the radiation pattern of left-lateral faulting, the strong directivity  
389 of the SW-oriented back rupture process can result in a further cascading of the rup-  
390 ture toward the SW. Our source model exhibits a relatively fast and smooth rupture along  
391 the section near Nurdağı, whilst it suddenly slows down at 55 s, where the rupture in-  
392 tersects at the apparent left-step in the active fault strand south of Hassa (Fig. 1). Al-  
393 though the SW-oriented rupture propagation and the deceleration of migration speed  
394 south of Hassa are robustly resolved, we refrain from discussing the potency rate found  
395 at the very beginning of the rupture episode 4 (at around ~0 km from the fault junction;  
396 Fig. 2c) because it is located close to the model boundary and its appearance is depen-  
397 dent on the assumption of duration of potency-rate functions (Fig. S10).

398 The strike extracted from the best-double-couple solution of our estimated potency-  
399 density tensors is not apparently aligned with the bulk linear trend of the active faults  
400 (Fig. 2). However, because we observe non-double-couple fractions for the SW end rup-  
401 ture (e.g., 24% during 60–61 s; Fig. 3), we cannot clearly define which individual fault  
402 strands likely ruptured. South of Hassa, several distinct fault segments are separated  
403 by step-overs (Fig. 3) (Duman & Emre, 2013). The aftershock distribution here is also  
404 more scattered than elsewhere along the main EAF and along the splay fault. These af-  
405 tershock patterns appear consistent between catalogs using different relocation meth-  
406 ods (Melgar et al., 2023; Lomax, 2023) (Fig. S8); however, we cannot rule out a greater  
407 earthquake location uncertainty due to diminished regional seismic network coverage  
408 close to the Syria border. Pre-earthquake field measurements (Emre et al., 2018; Duman  
409 & Emre, 2013), as well as the fault rupture mapping immediately after the 2023 earth-  
410 quakes (Reitman et al., 2023) show a zigzag geometry involving the bends and curves.  
411 This evidence collectively suggests that the later phase of rupture may have involved  
412 multiple faults with different geometries in the SW.

### 413 4.4 $M_W$ 7.6 event: curved and focused rupture

414 We find the  $M_W$  7.6 earthquake shows a much more focused rupture process, com-  
415 pared with the preceding  $M_W$  7.9 event. Yet, our solution finds that the strike of the rup-  
416 tured fault geometry curves gradually, with a counterclockwise rotation toward the west.  
417 The rotation trend can favorably be oriented to the optimal plane of the background hor-  
418 izontal stress given the bulk E-W oriented left-lateral strike-slip system of the Sürgü fault  
419 zone. This trend can thus favor rupture propagation, in a similar way to a fault-releasing  
420 bend (e.g., Kase & Day, 2006). In addition, such a favorably curved fault geometry may  
421 have facilitated the supershear rupture (e.g., Trugman & Dunham, 2014; Bruhat et al.,  
422 2016), albeit over a relatively short distance. At the western and eastern ends of the model  
423 domain, we find a significant change of mapped fault geometry and the orientation of

424 the potency density tensors. At these domains, the strike orientation is almost NS, and  
425 dip-slip faulting becomes dominant. The complex network in Göksun-Savrun faults to  
426 the west and Nurhak Fault complex to the east (Duman & Emre, 2013) can explain such  
427 the significant change of fault geometry, asymmetric nature of the bilateral rupture, and  
428 the likely reason for abrupt rupture termination at both ends.

429 The collocation of the two  $M_W$  7.9 and  $M_W$  7.6 earthquakes, only separated around  
430 9 hours apart, may give rise to a question over how the initial  $M_W$  7.9 earthquake can  
431 affect and possibly trigger the later  $M_W$  7.6 earthquake. Such earthquake doublets have  
432 been reported before in different tectonic environments (e.g., Lay & Kanamori, 1980;  
433 Astiz & Kanamori, 1984; Nissen et al., 2016; Ammon et al., 2008; Fan et al., 2016; Lay  
434 et al., 2013; ten Brink et al., 2020; Hicks & Rietbrock, 2015; Ross et al., 2019; Y. Jiang  
435 et al., 2022; Yagi et al., 2023). Our Coulomb stress analyses using our estimated source  
436 model shows the  $M_W$  7.9 earthquake may have induced positive static stress change in  
437 the hypothesized  $M_W$  7.6 source domain ( $\sim 0.4$  bar) (Fig. S6), which may have brought  
438 the fault that hosted the  $M_W$  7.6 earthquake closer to failure.

## 439 **Conclusions**

440 We find the differently oriented, curved, and multiple fault segments facilitate the  
441 series of complex rupture geometries during the devastating earthquakes in 2023. Back-  
442 propagating rupture with discrete interludes of rupture at supershear velocity during  
443 the initial  $M_W$  7.9 earthquake was facilitated by the branching fault rupture that pro-  
444 vided an initial stress trigger to the larger-scale main EAF rupture. The secondary  $M_W$  7.6  
445 earthquake involved a more continuous, westward-directed supershear rupture, which  
446 was abruptly interrupted by the geometric barriers in both the western and eastern ends  
447 of the northern strand of the EAF, being responsible for the relatively focused rupture  
448 extent. Our results suggest the geometrically complex fault network around the source  
449 region should be key to developing multi-scale cascading rupture growth and alternat-  
450 ing rupture directions, which will be critical inputs for both our understanding of earth-  
451 quake source physics and better assessment of the future damaging earthquakes in com-  
452 plex fault zones.

## 453 **Open Research**

454 Materials presented in this paper are archived and available at <https://doi.org/10.5281/zenodo.7678181>. The seismic data were downloaded through the IRIS Wilber 3 system  
455 ([https://ds.iris.edu/wilber3/find\\_event](https://ds.iris.edu/wilber3/find_event)) or IRIS Web Services (<https://service.iris.edu>).  
456 We used ObsPy (<https://doi.org/10.5281/zenodo.165135>; Beyreuther et al., 2010), Py-  
457 rocko (<https://pyrocko.org/>; Heimann et al., 2017), matplotlib (<https://doi.org/10.5281/zenodo.592536>;  
458 Hunter, 2007), Cartopy (<https://doi.org/10.5281/zenodo.1182735>; Met  
459 Office, 2015; Elson et al., 2022), Generic Mapping Tools (<https://doi.org/10.5281/zenodo.3407865>;  
460 Wessel & Luis, 2017); and Scientific colour maps (<https://doi.org/10.5281/zenodo.1243862>;  
461 Cramer, 2018; Cramer et al., 2020) for data processing and visual-  
462 ization. First motion mechanisms were picked using waveform data from the follow-  
463 ing seismic networks: KO (<https://doi.org/10.7914/SN/KO>); IM (<https://www.fdsn.org/>)

465 networks/detail/IM/); TK (<https://doi.org/10.7914/SN/TK>); and TU ([https://doi.org/](https://doi.org/10.7914/SN/TU)  
466 10.7914/SN/TU).

## 467 **Acknowledgments**

468 We thank the editor Germán Prieto and the reviewer Erdinc Saygin and the anonymous  
469 reviewer for their thorough evaluations and providing constructive comments and sug-  
470 gestions. We also thank Ahmed Ettaf Elbanna, František Gallovič, and Jiří Zahradník  
471 for fruitful discussion. The facilities of IRIS Data Services, and specifically the IRIS Data  
472 Management Center, were used for access to waveforms, related metadata, and/or de-  
473 rived products used in this study. IRIS Data Services are funded through the Seismo-  
474 logical Facilities for the Advancement of Geoscience (SAGE) Award of the National Sci-  
475 ence Foundation under Cooperative Support Agreement EAR-1851048. We appreciate  
476 the Disaster and Emergency Management Presidency of Türkiye (AFAD) for providing  
477 an initial catalogue of aftershocks and phase-arrival data acquired from their bulletin  
478 resources. This work was supported by JSPS Grant-in-Aid for Scientific Research (C) 19K04030  
479 and 22K03751, JSPS Early-Career Scientists 20K14570, and JSPS Grant-in-Aid for Spe-  
480 cial Purposes 22K21372. The authors declare no conflicts of interest relevant to this study.

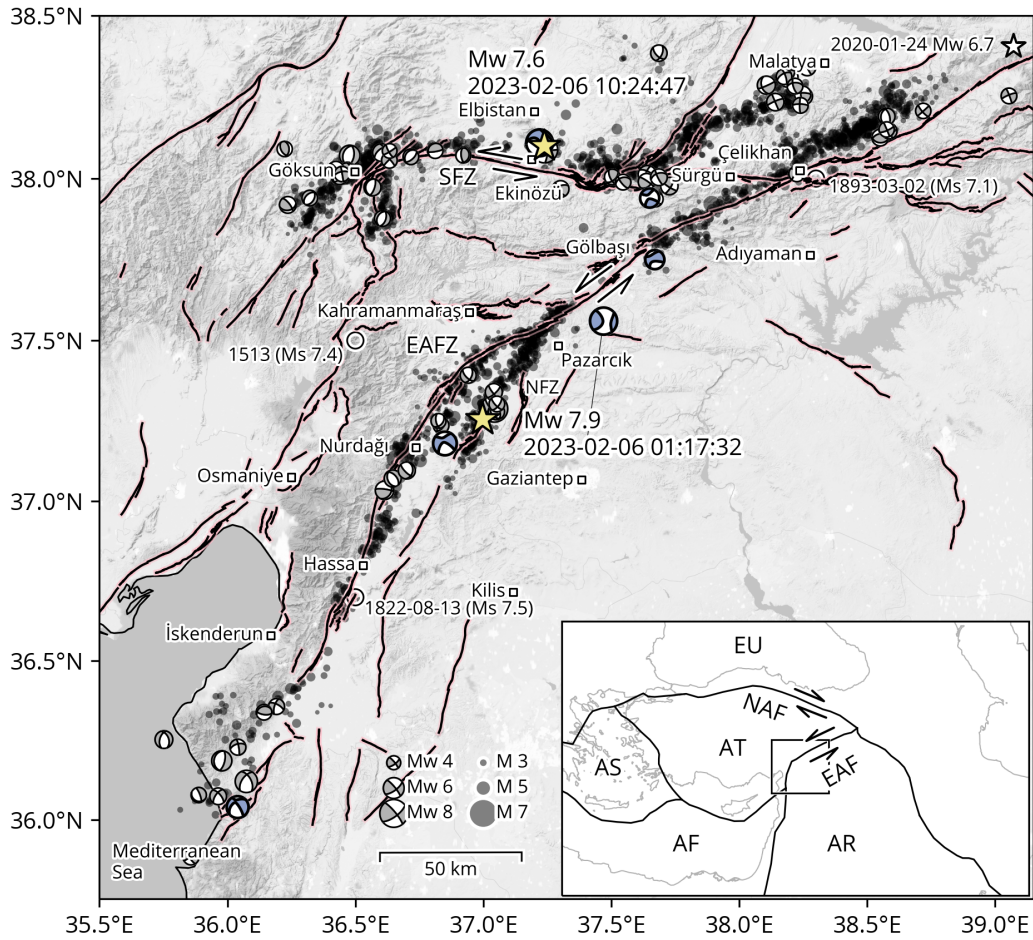


**Figure 1.** Summary of the study region. The yellow stars are the relocated epicenters of the  $M_W$  7.9 and  $M_W$  7.6 earthquakes. The dots are the relocated aftershocks ( $M \geq 1.1$ ) from 2023-02-06 01:17:32 (UTC) to 2023-02-16 21:35:55 (UTC) (after Melgar et al., 2023). The blue beachballs are the GCMT solutions (Dziewonski et al., 1981; Ekström et al., 2012) and the gray beachballs are the focal mechanisms determined by the AFAD (AFAD Focal Mechanism Solution, 2023) during the 2023 earthquake sequence. The active faults are from Emre et al. (2018), including the East Anatolian Fault Zone (EAFZ), Sürgü Fault Zone (SFZ), and Narlıdağ fault zone (NFZ). The square markers locate major provinces and towns. The white star is the epicenter of the 2020  $M_W$  6.7 Doğanyol–Sivrice earthquake (Taymaz et al., 2021). The circles are the epicenters of the historical earthquakes (Ambraseys, 1989; Ambraseys & Jackson, 1998). The basemap tiles (terrain) including the administrative boundaries are provided by Stamen Design (under CC BY 3.0 license) and OpenStreetMap (under ODbL license). The inset map shows the boundaries between Aegean Sea (AS), African (AF), Anatolian (AT), Arabian (AR), and Eurasian (EU) plates (Bird, 2003). The arrows denote the relative motion of the EAF and the NAF. The square box outlines the map extent of Fig. 1.

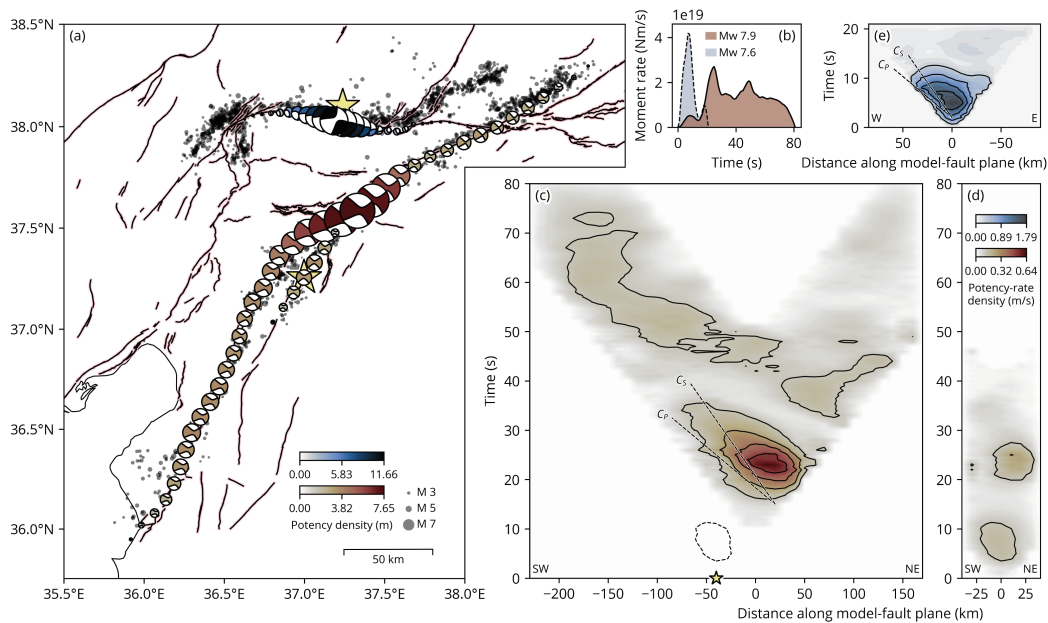


**Figure 2.** Summary of our solutions for the  $M_W$  7.9 and  $M_W$  7.6 earthquakes. (a) The beach-ball shows the lower-hemispheric projection of the moment tensor calculated by integrating the potency-rate density tensors with respect to time at each source element, with its size scaled with the potency density. Only the moment tensors with the maximum potency density along depth are shown. A full set of the potency-density tensors are shown in Fig. S4. The stars, dots, and lines are the same as shown in Fig. 1. (b) The moment-rate functions. The right panels show the spatiotemporal distributions of the potency-rate density for (c,d) the  $M_W$  7.9 and (e) the  $M_W$  7.6 earthquakes, projected along the non-planar model faults. The “0” on the X-axis of panel (c) corresponds to the location of junction between the splay fault and the main EAF, while “0” of panel (d) corresponds to the initial rupture point on the splay fault. The star shows the location of the source element on the EAF that is closest to the initial rupture point on the splay fault. The dashed contours show the potency-rate density on the splay fault during OT+0–15 s projected onto the approximate location on the main EAF model domain. The panel (d) is the splay fault domain for the  $M_W$  7.9 earthquake. The abscissa shows the distance along the model fault. The dashed lines of  $C_P$  (6.0 km/s) and  $C_S$  (3.5 km/s) represent the reference  $P$ - and  $S$ -wave velocities near the source region from the first layer of Table S1. The black contours are drawn at every 0.13 m/s (lower panels) and 0.36 m/s (upper panel) for the  $M_W$  7.9 and the  $M_W$  7.6 earthquakes, respectively. The panel (d) is flipped horizontally so that it can intuitively be compared with a map view of the corresponding model.

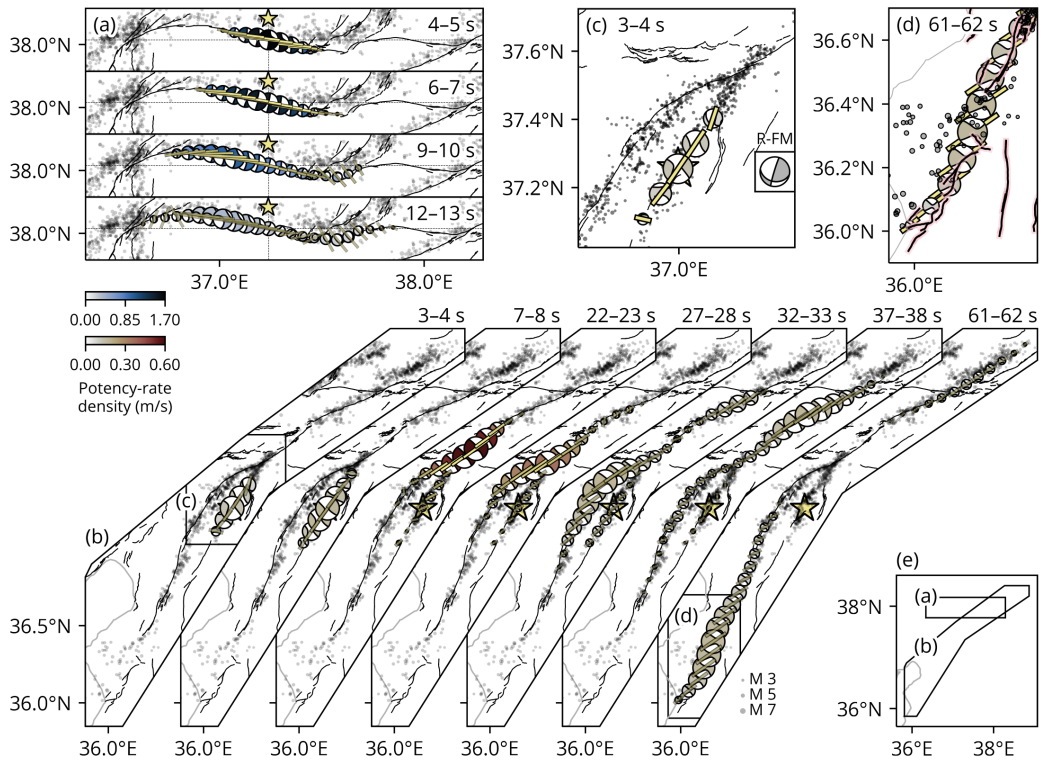


**Figure 3.** Selected snapshots of the spatiotemporal potency-rate density tensor distributions for (a) the  $M_W$  7.6 and (b)  $M_W$  7.9 earthquakes. The time window for the snapshot is shown on the corresponding panel. The yellow bar is the strike orientation extracted from the best-fitting double-couple components of the resultant potency-rate density tensors. The size of the beachball is scaled by the maximum potency-rate density in the corresponding time window. The optimum strike angle is one of the two possible nodal planes that minimizes the inner product of fault-normal vectors of the candidate plane and the reference fault plane:  $54^\circ/90^\circ$  and  $261^\circ/90^\circ$  (strike/dip) for the  $M_W$  7.9 and the  $M_W$  7.6 earthquakes, respectively. Only the source elements of the maximum potency-rate density along depth are shown. The full snapshots are shown in Movies S1–S3. Panels (c) and (d) show the enlarged view of the initial and fourth rupture episodes, respectively. The inset on (c) shows the best-fitting focal mechanism:  $197^\circ/86^\circ/56^\circ$  (strike/dip/rake) determined by first-motions recorded by seismometer and strong-motion stations up to 350 km away (see Open Research) using the method of Hardebeck and Shearer (2002) with takeoff angles computed in the velocity model of Melgar et al. (2020). The stars, dots, and lines are the same as shown in Fig. 1. Panel (e) shows the map extents of (a) and (b).

481

## References

482

Abdelmeguid, M., Zhao, C., Yalcinkaya, E., Gazetas, G., Elbanna, A., & Rosakis, A. J. (2023). Revealing The Dynamics of the Feb 6th 2023 M7.8 Kahramanmaraş/Pazarcik Earthquake: near-field records and dynamic rupture. *EarthArXiv*. doi:10.31223/X5066R

483

484

485

486

487

488

489

Abercrombie, R. E., Antolik, M., & Ekström, G. (2003). The June 2000 M w 7.9 earthquakes south of Sumatra: Deformation in the India-Australia Plate. *J. Geophys. Res. Solid Earth*, 108(B1), ESE 6–1–ESE 6–16. doi:10.1029/2001jb000674

490

491

492

493

494

495

496

AFAD. (2023). *AFAD (Disaster and Emergency Management Presidency) Earthquake Catalog*. Retrieved from <https://deprem.afad.gov.tr/event-catalog>

AFAD Focal Mechanism Solution. (2023). AFAD Focal Mechanism Solution. Retrieved from <https://deprem.afad.gov.tr/event-focal-mechanism>

Akaike, H. (1980). Likelihood and the Bayes procedure. *Trab. Estad. Y Investig. Oper.*, 31(1), 143–166. Retrieved from <https://doi.org/10.1007/BF02888350> doi:10.1007/BF02888350

497

498

499

500

501

Aktug, B., Ozener, H., Dogru, A., Sabuncu, A., Turgut, B., Halicioglu, K., ... Havazli, E. (2016). Slip rates and seismic potential on the East Anatolian Fault System using an improved GPS velocity field. *J. Geodyn.*, 94-95, 1–12. Retrieved from <http://dx.doi.org/10.1016/j.jog.2016.01.001><https://linkinghub.elsevier.com/retrieve/pii/S0264370716300102> doi:10.1016/j.jog.2016.01.001

502

503

504

505

Ambraseys, N. N. (1989). Temporary seismic quiescence: SE Turkey. *Geophys. J. Int.*, 96(2), 311–331. Retrieved from <https://academic.oup.com/gji/article-lookup/doi/10.1111/j.1365-246X.1989.tb04453.x> doi:10.1111/j.1365-246X.1989.tb04453.x

506

507

508

509

Ambraseys, N. N., & Jackson, J. A. (1998). Faulting associated with historical and recent earthquakes in the Eastern Mediterranean region. *Geophys. J. Int.*, 133(2), 390–406. Retrieved from <https://academic.oup.com/gji/article/133/2/390/578275> doi:10.1046/j.1365-246X.1998.00508.x

510

511

512

513

Ammon, C. J., Kanamori, H., & Lay, T. (2008). A great earthquake doublet and seismic stress transfer cycle in the central Kuril islands. *Nature*, 451(7178), 561–565. Retrieved from <http://www.nature.com/articles/nature06521> doi:10.1038/nature06521

514

515

516

517

Ando, R., Shaw, B. E., & Scholz, C. H. (2009). Quantifying Natural Fault Geometry: Statistics of Splay Fault Angles. *Bull. Seismol. Soc. Am.*, 99(1), 389–395. Retrieved from <https://pubs.geoscienceworld.org/bssa/article/99/1/389-395/350160> doi:10.1785/0120080942

518

519

520

521

Ando, R., & Yamashita, T. (2007). Effects of mesoscopic-scale fault structure on dynamic earthquake ruptures: Dynamic formation of geometrical complexity of earthquake faults. *J. Geophys. Res. Solid Earth*, 112(9), 1–15. doi:10.1029/2006JB004612

522

523

524

525

Aochi, H., Fukuyama, E., & Matsu'ura, M. (2000). Selectivity of spontaneous rupture propagation on a branched fault. *Geophys. Res. Lett.*, 27(22), 3635–3638. Retrieved from <http://doi.wiley.com/10.1029/2000GL011560> doi:10.1029/2000GL011560

526

Arpat, E., & Saroglu, F. (1972). The East Anatolian fault system; thoughts on its de-



- 527           velopment. *Miner. Res. Explor. Inst. Turkey*, 78, 33–39. Retrieved from [https://](https://dergipark.org.tr/en/pub/bulletinofmre/issue/3904/52066)  
528           dergipark.org.tr/en/pub/bulletinofmre/issue/3904/52066
- 529   Astiz, L., & Kanamori, H. (1984). An earthquake doublet in Ometepec, Guerrero,  
530           Mexico. *Phys. Earth Planet. Inter.*, 34(1-2), 24–45. Retrieved from [https://](https://linkinghub.elsevier.com/retrieve/pii/0031920184900827)  
531           linkinghub.elsevier.com/retrieve/pii/0031920184900827 doi:10.1016/0031-  
532           9201(84)90082-7
- 533   Bao, H., Ampuero, J.-P., Meng, L., Fielding, E. J., Liang, C., Milliner, C. W. D., ...  
534           Huang, H. (2019). Early and persistent supershear rupture of the 2018  
535           magnitude 7.5 Palu earthquake. *Nat. Geosci.*, 12(3), 200–205. Retrieved  
536           from <http://dx.doi.org/10.1038/s41561-018-0297-z>  
537           [http://www.nature.com/](http://www.nature.com/articles/s41561-018-0297-z)  
538           articles/s41561-018-0297-z doi:10.1038/s41561-018-0297-z
- 539   Barbot, S., Luo, H., Wang, T., Hamiel, Y., Piatibratova, O., Javed, M. T., ... Gurbuz,  
540           G. (2023). Slip distribution of the February 6, 2023 Mw 7.8 and Mw 7.6,  
541           Kahramanmaraş, Turkey earthquake sequence in the East Anatolian Fault  
542           Zone. *Seismica*, 2(3). Retrieved from [https://seismica.library.mcgill.ca/article/](https://seismica.library.mcgill.ca/article/view/502)  
543           view/502 doi:10.26443/seismica.v2i3.502
- 544   Beyreuther, M., Barsch, R., Krischer, L., Megies, T., Behr, Y., & Wassermann, J.  
545           (2010). ObsPy: A Python Toolbox for Seismology. *Seismol. Res. Lett.*, 81(3),  
546           530–533. doi:10.1785/gssrl.81.3.530
- 547   Bhat, H. S., Olives, M., Dmowska, R., & Rice, J. R. (2007). Role of fault  
548           branches in earthquake rupture dynamics. *J. Geophys. Res.*, 112(B11),  
549           B11309. Retrieved from <http://doi.wiley.com/10.1029/2007JB005027>  
550           doi:10.1029/2007JB005027
- 551   Bird, P. (2003). An updated digital model of plate boundaries. *Geochemistry, Geo-*  
552           *phys. Geosystems*, 4(3), 1105. doi:10.1029/2001GC000252
- 553   Bruhat, L., Fang, Z., & Dunham, E. M. (2016). Rupture complexity and the super-  
554           shear transition on rough faults. *J. Geophys. Res. Solid Earth*, 121(1), 210–224.  
555           doi:10.1002/2015JB012512
- 556   Crameri, F. (2018). Geodynamic diagnostics, scientific visualisation and StagLab  
557           3.0. *Geosci. Model Dev.*, 11(6), 2541–2562. doi:10.5194/gmd-11-2541-2018
- 558   Crameri, F., Shephard, G. E., & Heron, P. J. (2020). The misuse of colour in science  
559           communication. *Nat. Commun.*, 11(1), 5444. doi:10.1038/s41467-020-19160-  
560           7
- 561   Dal Zilio, L., & Ampuero, J.-p. (2023). Earthquake doublet in Turkey and Syria.  
562           *Commun. Earth Environ.*, 4(1), 71. Retrieved from [https://www.nature.com/](https://www.nature.com/articles/s43247-023-00747-z)  
563           articles/s43247-023-00747-z doi:10.1038/s43247-023-00747-z
- 564   Das, S., & Aki, K. (1977). Fault plane with barriers: A versatile earthquake model.  
565           *J. Geophys. Res.*, 82(36), 5658–5670. Retrieved from [http://doi.wiley.com/10](http://doi.wiley.com/10.1029/JB082i036p05658)  
566           .1029/JB082i036p05658 doi:10.1029/JB082i036p05658
- 567   Delouis, B., van den Ende, M., & Ampuero, J.-P. (2023). Kinematic rup-  
568           ture model of the February 6th 2023 Mw7.8 Turkey earthquake from  
569           a large set of near-source strong motion records combined by GNSS  
570           offsets reveals intermittent supershear rupture. *ESS Open Arch.*.  
571           doi:10.22541/essoar.168286647.71550161/v1
- 572   Duman, T. Y., Elmacı, H., Özalp, S., Kürçer, A., Kara, M., Özdemir, E., ... Uygun  
573           Güldoğan, Ç. (2020). Paleoseismology of the western Sürgü–Misis fault

- 573 system: East Anatolian Fault, Turkey. *Mediterr. Geosci. Rev.*, 2(3), 411–  
574 437. Retrieved from <https://doi.org/10.1007/s42990-020-00041-6>  
575 [link.springer.com/10.1007/s42990-020-00041-6](https://link.springer.com/10.1007/s42990-020-00041-6) doi:10.1007/s42990-020-  
576 00041-6
- 577 Duman, T. Y., & Emre, Ö. (2013). The East Anatolian Fault: geometry, segmen-  
578 tation and jog characteristics. *Geol. Soc. London, Spec. Publ.*, 372(1), 495–  
579 529. Retrieved from <https://www.lyellcollection.org/doi/10.1144/SP372.14>  
580 doi:10.1144/SP372.14
- 581 Dziewonski, A. M., Chou, T.-A., & Woodhouse, J. H. (1981). Determination of  
582 earthquake source parameters from waveform data for studies of global  
583 and regional seismicity. *J. Geophys. Res. Solid Earth*, 86(B4), 2825–2852.  
584 doi:10.1029/JB086iB04p02825
- 585 Ekström, G., Nettles, M., & Dziewoński, A. (2012). The global CMT project  
586 2004–2010: Centroid-moment tensors for 13,017 earthquakes. *Phys. Earth  
587 Planet. Inter.*, 200–201, 1–9. doi:10.1016/j.pepi.2012.04.002
- 588 Elson, P., de Andrade, E. S., Lucas, G., May, R., Hattersley, R., Campbell, E., ...  
589 daryl herzmann (2022). *Scitools/cartopy: v0.21.1*. Zenodo. Retrieved from  
590 <https://doi.org/10.5281/zenodo.7430317> doi:10.5281/zenodo.7430317
- 591 Emre, Ö., Duman, T. Y., Özalp, S., Şaroğlu, F., Olgun, , Elmacı, H., & Çan, T.  
592 (2018). Active fault database of Turkey. *Bull. Earthq. Eng.*, 16(8), 3229–3275.  
593 doi:10.1007/s10518-016-0041-2
- 594 Fan, W., Okuwaki, R., Barbour, A. J., Huang, Y., Lin, G., & Cochran, E. S. (2022).  
595 Fast rupture of the 2009 M w 6.9 Canal de Ballenas earthquake in the  
596 Gulf of California dynamically triggers seismicity in California. *Geo-  
597 phys. J. Int.*, 230(1), 528–541. Retrieved from <https://doi.org/10.1093/gji/ggac059>  
598 <https://academic.oup.com/gji/article/230/1/528/6524846>  
599 doi:10.1093/gji/ggac059
- 600 Fan, W., Shearer, P. M., Ji, C., & Bassett, D. (2016). Multiple branching rupture of  
601 the 2009 Tonga-Samoa earthquake. *J. Geophys. Res. Solid Earth*, 121(8), 5809–  
602 5827. doi:10.1002/2016JB012945
- 603 Fang, J., Ou, Q., Wright, T. J., Okuwaki, R., Amey, R. M. J., Craig, T. J., ... Magh-  
604 soudi, Y. (2022). Earthquake Cycle Deformation Associated With the 2021 M  
605 W 7.4 Maduo (Eastern Tibet) Earthquake: An Intrablock Rupture Event on a  
606 Slow-Slipping Fault From Sentinel-1 InSAR and Teleseismic Data. *J. Geophys.  
607 Res. Solid Earth*, 127(11). Retrieved from <https://onlinelibrary.wiley.com/doi/10.1029/2022JB024268>  
608 doi:10.1029/2022JB024268
- 609 Fliss, S., Bhat, H. S., Dmowska, R., & Rice, J. R. (2005). Fault branching and rupture  
610 directivity. *J. Geophys. Res. Solid Earth*, 110(B6). Retrieved from <https://doi.org/10.1029/2004JB003368>  
611 doi:https://doi.org/10.1029/2004JB003368
- 612 Fukahata, Y., & Wright, T. J. (2008). A non-linear geodetic data inversion us-  
613 ing ABIC for slip distribution on a fault with an unknown dip angle. *Geo-  
614 phys. J. Int.*, 173(2), 353–364. Retrieved from [https://academic.oup.com/gji/  
615 article-lookup/doi/10.1111/j.1365-246X.2007.03713.x](https://academic.oup.com/gji/article-lookup/doi/10.1111/j.1365-246X.2007.03713.x) doi:10.1111/j.1365-  
616 246X.2007.03713.x
- 617 Gallovič, F., Zahradník, J., Plicka, V., Sokos, E., Evangelidis, C., Fountoulakis, I., &  
618 Turhan, F. (2020). Complex rupture dynamics on an immature fault during

- 619 the 2020 Mw 6.8 Elazığ earthquake, Turkey. *Commun. Earth Environ.*, 1(1),  
620 40. Retrieved from <https://www.nature.com/articles/s43247-020-00038-x>  
621 doi:10.1038/s43247-020-00038-x
- 622 Hall, S. (2023). What Turkey's earthquake tells us about the science of seismic fore-  
623 casting. *Nature*, 615(7952), 388–389. Retrieved from [https://documentation](https://documentation.sisense.com/latest/creating-dashboards/forecast.htm#gsc.tab=0)  
624 [www.nature.com/articles/d41586-023-00685-y](https://www.nature.com/articles/d41586-023-00685-y) doi:10.1038/d41586-023-  
625 00685-y
- 626
- 627 Hardebeck, J. L., & Shearer, P. M. (2002). A New Method for Determin-  
628 ing First-Motion Focal Mechanisms. *Bull. Seismol. Soc. Am.*, 92(6),  
629 2264–2276. Retrieved from <https://doi.org/10.1785/0120010200>  
630 doi:10.1785/0120010200
- 631 Hartzell, S. H., & Heaton, T. H. (1983). Inversion of strong ground motion and  
632 teleseismic waveform data for the fault rupture history of the 1979 Imperial  
633 Valley, California, earthquake. *Bull. Seismol. Soc. Am.*, 73(6A), 1553–1583.  
634 doi:10.1785/BSSA07306A1553
- 635 Heimann, S., Kriegerowski, M., Isken, M., Cesca, S., Daout, S., Grigoli, F., ...  
636 Vasyura-Bathke, H. (2017). *Pyrocko - An open-source seismology toolbox and*  
637 *library*. GFZ Data Services. doi:10.5880/GFZ.2.1.2017.001
- 638 Hicks, S. P., Okuwaki, R., Steinberg, A., Rychert, C. A., Harmon, N., Abercrom-  
639 bie, R. E., ... Sudhaus, H. (2020). Back-propagating supershear rupture in  
640 the 2016 Mw 7.1 Romanche transform fault earthquake. *Nat. Geosci.*, 13(9),  
641 647–653. doi:10.1038/s41561-020-0619-9
- 642 Hicks, S. P., & Rietbrock, A. (2015). Seismic slip on an upper-plate normal fault  
643 during a large subduction megathrust rupture. *Nat. Geosci.*, 8(12), 955–960.  
644 doi:10.1038/ngeo2585
- 645 Hu, Y., Yagi, Y., Okuwaki, R., & Shimizu, K. (2021). Back-propagating rup-  
646 ture evolution within a curved slab during the 2019 Mw 8.0 Peru in-  
647 traslab earthquake. *Geophys. J. Int.*, 227(3), 1602–1611. Retrieved from  
648 [https://academic.oup.com/gji/advance-article/doi/10.1093/gji/ggab303/](https://academic.oup.com/gji/advance-article/doi/10.1093/gji/ggab303/6338111)  
649 [6338111](https://academic.oup.com/gji/article/227/3/1602/6338111)<https://academic.oup.com/gji/article/227/3/1602/6338111>  
650 doi:10.1093/gji/ggab303
- 651 Huang, Y. (2018). Earthquake Rupture in Fault Zones With Along-Strike  
652 Material Heterogeneity. *J. Geophys. Res. Solid Earth*, 123(11), 9884–  
653 9898. Retrieved from <http://doi.wiley.com/10.1029/2018JB016354>  
654 doi:10.1029/2018JB016354
- 655 Hunter, J. D. (2007). Matplotlib: A 2D Graphics Environment. *Comput. Sci. Eng.*,  
656 9(3), 90–95. doi:10.1109/MCSE.2007.55
- 657 Hussain, E., Kalaycıoğlu, S., Milliner, C. W. D., & Çakir, Z. (2023). Preconditioning  
658 the 2023 Kahramanmaraş (Türkiye) earthquake disaster. *Nat. Rev. Earth Envi-*  
659 *ron.*, 5–7. Retrieved from [https://www.nature.com/articles/s43017-023-00411-](https://www.nature.com/articles/s43017-023-00411-2)  
660 [2](https://www.nature.com/articles/s43017-023-00411-2) doi:10.1038/s43017-023-00411-2
- 661 Ide, S., & Aochi, H. (2005). Earthquakes as multiscale dynamic ruptures with het-  
662 erogeneous fracture surface energy. *J. Geophys. Res. Solid Earth*, 110(B11),  
663 1–10. Retrieved from <http://doi.wiley.com/10.1029/2004JB003591>  
664 doi:10.1029/2004JB003591

- 665 Ishii, M., Shearer, P. M., Houston, H., & Vidale, J. E. (2005). Extent, duration and  
666 speed of the 2004 Sumatra-Andaman earthquake imaged by the Hi-Net array.  
667 *Nature*, 435(7044), 933–936. doi:10.1038/nature03675
- 668 Jackson, J., & McKenzie, D. (1984). Active tectonics of the Alpine–Himalayan  
669 Belt between western Turkey and Pakistan. *Geophys. J. Int.*, 77(1), 185–264.  
670 Retrieved from [https://academic.oup.com/gji/article-lookup/doi/10.1111/  
671 j.1365-246X.1984.tb01931.x](https://academic.oup.com/gji/article-lookup/doi/10.1111/j.1365-246X.1984.tb01931.x) doi:10.1111/j.1365-246X.1984.tb01931.x
- 672 Jiang, X., Song, X., Li, T., & Wu, K. (2023). Moment Magnitudes of Two Large Turk-  
673 ish Earthquakes in February 2023 from Long-Period Coda. *KeAi Earthq. Sci.*  
674 doi:10.2139/ssrn.4361747
- 675 Jiang, Y., González, P. J., & Bürgmann, R. (2022). Subduction earthquakes con-  
676 trolled by incoming plate geometry: The 2020  $M > 7.5$  Shumagin, Alaska,  
677 earthquake doublet. *Earth Planet. Sci. Lett.*, 584, 117447. Retrieved  
678 from <https://linkinghub.elsevier.com/retrieve/pii/S0012821X22000838>  
679 doi:10.1016/j.epsl.2022.117447
- 680 Kame, N., Rice, J. R., & Dmowska, R. (2003). Effects of prestress state and rup-  
681 ture velocity on dynamic fault branching. *J. Geophys. Res. Solid Earth*,  
682 108(B5), 1–21. Retrieved from <http://doi.wiley.com/10.1029/2002JB002189>  
683 doi:10.1029/2002JB002189
- 684 Kase, Y., & Day, S. M. (2006). Spontaneous rupture processes on a bending fault.  
685 *Geophys. Res. Lett.*, 33(10), 1–4. Retrieved from [http://doi.wiley.com/10.1029/  
686 2006GL025870](http://doi.wiley.com/10.1029/2006GL025870) doi:10.1029/2006GL025870
- 687 Kennett, B. L., Engdahl, E. R., & Buland, R. (1995). Constraints on seismic ve-  
688 locities in the Earth from traveltimes. *Geophys. J. Int.*, 122(1), 108–124.  
689 doi:10.1111/j.1365-246X.1995.tb03540.x
- 690 Kikuchi, M., & Kanamori, H. (1991). Inversion of complex body waves-III. *Bull.*  
691 *Seism. Soc. Am.*, 81(6), 2335–2350. doi:10.1785/BSSA0810062335
- 692 King, G. C., Stein, R. S., & Lin, J. (1994). Static stress changes and the  
693 triggering of earthquakes. *Bull. Seismol. Soc. Am.*, 84(3), 935–953.  
694 doi:10.1785/BSSA0840030935
- 695 Laske, G., Masters, T. G., Ma, Z., & Pasyanos, M. (2013). Update on CRUST1.0 - A 1-  
696 degree Global Model of Earth's Crust. *Geophys. Res. Abstr.* 15, *Abstr. EGU2013-*  
697 *2658*, 15, Abstract EGU2013–2658. ([https://igppweb.ucsd.edu/~gabi/crust1  
698 .html](https://igppweb.ucsd.edu/~gabi/crust1.html))
- 699 Lay, T., Duputel, Z., Ye, L., & Kanamori, H. (2013). The December 7, 2012 Japan  
700 Trench intraplate doublet ( $M_w$  7.2, 7.1) and interactions between near-  
701 trench intraplate thrust and normal faulting. *Phys. Earth Planet. Inter.*,  
702 220, 73–78. Retrieved from [https://linkinghub.elsevier.com/retrieve/pii/  
703 S0031920113000599](https://linkinghub.elsevier.com/retrieve/pii/S0031920113000599) doi:10.1016/j.pepi.2013.04.009
- 704 Lay, T., & Kanamori, H. (1980). Earthquake doublets in the Solomon Islands. *Phys.*  
705 *Earth Planet. Inter.*, 21(4), 283–304. Retrieved from [https://linkinghub.elsevier  
706 .com/retrieve/pii/003192018090134X](https://linkinghub.elsevier.com/retrieve/pii/003192018090134X) doi:10.1016/0031-9201(80)90134-X
- 707 Lin, J., & Stein, R. S. (2004). Stress triggering in thrust and subduction earth-  
708 quakes and stress interaction between the southern San Andreas and nearby  
709 thrust and strike-slip faults. *J. Geophys. Res. Solid Earth*, 109(B2), 1–19.  
710 doi:10.1029/2003jb002607

- 711 Lomax, A. (2023). *Precise, NLL-SSST-coherence hypocenter catalog for the 2023 Mw 7.8*  
712 *and Mw 7.6 SE Turkey earthquake sequence*. Zenodo. Retrieved from [https://doi](https://doi.org/10.5281/zenodo.7727678)  
713 [.org/10.5281/zenodo.7727678](https://doi.org/10.5281/zenodo.7727678) doi:10.5281/zenodo.7727678
- 714 Mai, P. M., Aspiotis, T., Aquib, T. A., Cano, E. V., Castro-Cruz, D., Espindola-  
715 Carmona, A., . . . Jónsson, S. (2023). The Destructive Earthquake Dou-  
716 blet of 6 February 2023 in South-Central Türkiye and Northwestern Syria:  
717 Initial Observations and Analyses. *Seism. Rec.*, 3(2), 105–115. Retrieved  
718 from [https://pubs.geoscienceworld.org/tsr/article/3/2/105/623200/The](https://pubs.geoscienceworld.org/tsr/article/3/2/105/623200/The-Destructive-Earthquake-Doublet-of-6-February)  
719 [-Destructive-Earthquake-Doublet-of-6-February](https://pubs.geoscienceworld.org/tsr/article/3/2/105/623200/The-Destructive-Earthquake-Doublet-of-6-February) doi:10.1785/0320230007
- 720 McKenzie, D. (1972). Active Tectonics of the Mediterranean Region. *Geophys.*  
721 *J. Int.*, 30(2), 109–185. Retrieved from [https://academic.oup.com/gji/](https://academic.oup.com/gji/article-lookup/doi/10.1111/j.1365-246X.1972.tb02351.x)  
722 [article-lookup/doi/10.1111/j.1365-246X.1972.tb02351.x](https://academic.oup.com/gji/article-lookup/doi/10.1111/j.1365-246X.1972.tb02351.x) doi:10.1111/j.1365-  
723 246X.1972.tb02351.x
- 724 Melgar, D., Ganas, A., Taymaz, T., Valkaniotis, S., Crowell, B. W., Kapetani-  
725 dis, V., . . . Öcalan, T. (2020). Rupture kinematics of 2020 January 24  
726 Mw 6.7 Doğanyol-Sivrice, Turkey earthquake on the East Anatolian Fault  
727 Zone imaged by space geodesy. *Geophys. J. Int.*, 223(2), 862–874. Re-  
728 trieved from <https://academic.oup.com/gji/article/223/2/862/5872486>  
729 [doi:10.1093/gji/ggaa345](https://academic.oup.com/gji/article/223/2/862/5872486)
- 730 Melgar, D., Taymaz, T., Ganas, A., Crowell, B., Öcalan, T., Kahraman, M., . . . Al-  
731 tuntun, C. (2023). Sub- and super-shear ruptures during the 2023 Mw  
732 7.8 and Mw 7.6 earthquake doublet in SE Türkiye. *Seismica*, 2(3), 1–14.  
733 doi:10.26443/seismica.v2i3.387
- 734 Meng, L., Ampuero, J. P., Stock, J., Duputel, Z., Luo, Y., & Tsai, V. C. (2012).  
735 Earthquake in a maze: Compressional rupture branching during the  
736 2012 Mw 8.6 Sumatra earthquake. *Science*, 337(6095), 724–726.  
737 doi:10.1126/science.1224030
- 738 Meng, L., Bao, H., Huang, H., Zhang, A., Bloore, A., & Liu, Z. (2018). Double  
739 pincer movement: Encircling rupture splitting during the 2015 Mw 8.3 Il-  
740 lapel earthquake. *Earth Planet. Sci. Lett.*, 495, 164–173. Retrieved from  
741 <https://doi.org/10.1016/j.epsl.2018.04.057> doi:10.1016/j.epsl.2018.04.057
- 742 Met Office. (2015). *Cartopy: a cartographic python library with a Mat-*  
743 *plotlib interface*. Retrieved from <https://scitools.org.uk/cartopy>  
744 [doi:10.5281/zenodo.1182735](https://scitools.org.uk/cartopy)
- 745 Nissen, E., Elliott, J. R., Sloan, R. A., Craig, T. J., Funning, G. J., Hutko, A., . . .  
746 Wright, T. J. (2016). Limitations of rupture forecasting exposed by in-  
747 stantaneously triggered earthquake doublet. *Nat. Geosci.*, 9(4), 330–336.  
748 doi:10.1038/ngeo2653
- 749 Okubo, K., Rougier, E., Lei, Z., & Bhat, H. S. (2020). Modeling earthquakes with  
750 off-fault damage using the combined finite-discrete element method. *Com-*  
751 *put. Part. Mech.*, 7(5), 1057–1072. Retrieved from [https://doi.org/10.1007/](https://doi.org/10.1007/s40571-020-00335-4)  
752 [s40571-020-00335-4](https://doi.org/10.1007/s40571-020-00335-4)<https://link.springer.com/10.1007/s40571-020-00335-4>  
753 [doi:10.1007/s40571-020-00335-4](https://link.springer.com/10.1007/s40571-020-00335-4)
- 754 Okuwaki, R., & Fan, W. (2022). Oblique Convergence Causes Both Thrust and  
755 Strike-Slip Ruptures During the 2021 M 7.2 Haiti Earthquake. *Geophys.*  
756 *Res. Lett.*, 49(2), 1–12. Retrieved from <https://onlinelibrary.wiley.com/doi/>

- 10.1029/2021GL096373 doi:10.1029/2021GL096373
- 757  
758 Okuwaki, R., Hicks, S. P., Craig, T. J., Fan, W., Goes, S., Wright, T. J., & Yagi, Y.  
759 (2021). Illuminating a Contorted Slab With a Complex Intraslab Rupture Evo-  
760 lution During the 2021 Mw 7.3 East Cape, New Zealand Earthquake. *Geophys.*  
761 *Res. Lett.*, *48*(24), 1–13. Retrieved from [https://onlinelibrary.wiley.com/doi/](https://onlinelibrary.wiley.com/doi/10.1029/2021GL095117)  
762 [10.1029/2021GL095117](https://onlinelibrary.wiley.com/doi/10.1029/2021GL095117) doi:10.1029/2021GL095117
- 763 Okuwaki, R., Hirano, S., Yagi, Y., & Shimizu, K. (2020). Inchworm-like source  
764 evolution through a geometrically complex fault fueled persistent supershear  
765 rupture during the 2018 Palu Indonesia earthquake. *Earth Planet. Sci. Lett.*,  
766 *547*, 116449. doi:10.1016/j.epsl.2020.116449
- 767 Okuwaki, R., Yagi, Y., Aránguiz, R., González, J., & González, G. (2016). Rupture  
768 Process During the 2015 Illapel, Chile Earthquake: Zigzag-Along-Dip Rupture  
769 Episodes. *Pure Appl. Geophys.*, *173*(4), 1011–1020. doi:10.1007/s00024-016-  
770 1271-6
- 771 Olson, A. H., & Apsel, R. J. (1982). Finite faults and inverse theory with applications  
772 to the 1979 Imperial Valley earthquake. *Bull. Seismol. Soc. Am.*, *72*(6A), 1969–  
773 2001. Retrieved from + doi:10.1785/BSSA07206A1969
- 774 Otsuki, K., & Dilov, T. (2005). Evolution of hierarchical self-similar geometry of  
775 experimental fault zones: Implications for seismic nucleation and earthquake  
776 size. *J. Geophys. Res. Solid Earth*, *110*(3), 1–9. doi:10.1029/2004JB003359
- 777 Perinçek, D., & Çemen, I. (1990). The structural relationship between the East  
778 Anatolian and Dead Sea fault zones in southeastern Turkey. *Tectonophysics*,  
779 *172*(3-4), 331–340. Retrieved from [https://linkinghub.elsevier.com/retrieve/](https://linkinghub.elsevier.com/retrieve/pii/004019519090039B)  
780 [pii/004019519090039B](https://linkinghub.elsevier.com/retrieve/pii/004019519090039B) doi:10.1016/0040-1951(90)90039-B
- 781 Pousse-Beltran, L., Nissen, E., Bergman, E. A., Cambaz, M. D., Gaudreau, É.,  
782 Karasözen, E., & Tan, F. (2020). The 2020 M w 6.8 Elazığ (Turkey) Earth-  
783 quake Reveals Rupture Behavior of the East Anatolian Fault. *Geophys. Res.*  
784 *Lett.*, *47*(13), 1–14. Retrieved from [https://onlinelibrary.wiley.com/doi/](https://onlinelibrary.wiley.com/doi/10.1029/2020GL088136)  
785 [10.1029/2020GL088136](https://onlinelibrary.wiley.com/doi/10.1029/2020GL088136) doi:10.1029/2020GL088136
- 786 Ragon, T., Simons, M., Bletery, Q., Cavalié, O., & Fielding, E. (2021). A Stochastic  
787 View of the 2020 Elazığ M w 6.8 Earthquake (Turkey). *Geophys. Res. Lett.*,  
788 *48*(3), 1–13. Retrieved from [https://onlinelibrary.wiley.com/doi/10.1029/](https://onlinelibrary.wiley.com/doi/10.1029/2020GL090704)  
789 [2020GL090704](https://onlinelibrary.wiley.com/doi/10.1029/2020GL090704) doi:10.1029/2020GL090704
- 790 Reitman, N. G., Briggs, R. W., Barnhart, W. D., Thompson Jobe, J. A., DuRoss, C. B.,  
791 Hatem, A. E., ... Mejstrik, J. D. (2023). Preliminary fault rupture mapping of  
792 the 2023 M7.8 and M7.5 Türkiye Earthquakes.  
793 doi:10.5066/P985I7U2
- 794 Rosakis, A. J., Abdelmeguid, M., & Elbanna, A. (2023). Evidence of Early Su-  
795 pershear Transition in the Feb 6th 2023 Mw 7.8 Kahramanmaraş Turkey  
796 Earthquake From Near-Field Records. *EarthArXiv*. doi:10.31223/X5W95G
- 797 Ross, Z. E., Idini, B., Jia, Z., Stephenson, O. L., Zhong, M., Wang, X., ... Jung, J.  
798 (2019). Hierarchical interlocked orthogonal faulting in the 2019 Ridge-  
799 crest earthquake sequence. *Science (80-. )*, *366*(6463), 346–351. Re-  
800 trieved from <https://www.science.org/doi/10.1126/science.aaz0109>  
801 doi:10.1126/science.aaz0109

- 802 Ruppert, N. A., Rollins, C., Zhang, A., Meng, L., Holtkamp, S. G., West, M. E., &  
803 Freymueller, J. T. (2018). Complex Faulting and Triggered Rupture During the  
804 2018 MW 7.9 Offshore Kodiak, Alaska, Earthquake. *Geophys. Res. Lett.*, *45*(15),  
805 7533–7541. doi:10.1029/2018GL078931
- 806 Sato, D., Fukahata, Y., & Nozue, Y. (2022). Appropriate reduction of the poste-  
807 rior distribution in fully Bayesian inversions. *Geophys. J. Int.*, *231*(2), 950–981.  
808 doi:10.1093/gji/ggac231
- 809 Satriano, C., Kiraly, E., Bernard, P., & Vilotte, J.-P. (2012). The 2012 Mw 8.6 Suma-  
810 tra earthquake: Evidence of westward sequential seismic ruptures associ-  
811 ated to the reactivation of a N-S ocean fabric. *Geophys. Res. Lett.*, *39*(15).  
812 doi:10.1029/2012GL052387
- 813 Scholz, C. H., Ando, R., & Shaw, B. E. (2010). The mechanics of first order splay  
814 faulting: The strike-slip case. *J. Struct. Geol.*, *32*(1), 118–126. Retrieved from  
815 <http://dx.doi.org/10.1016/j.jsg.2009.10.007>[https://linkinghub.elsevier.com/](https://linkinghub.elsevier.com/retrieve/pii/S0191814109002211)  
816 [retrieve/pii/S0191814109002211](https://linkinghub.elsevier.com/retrieve/pii/S0191814109002211) doi:10.1016/j.jsg.2009.10.007
- 817 Shimizu, K., Yagi, Y., Okuwaki, R., & Fukahata, Y. (2020). Development of an inver-  
818 sion method to extract information on fault geometry from teleseismic data.  
819 *Geophys. J. Int.*, *220*(2), 1055–1065. doi:10.1093/gji/ggz496
- 820 Socquet, A., Hollingsworth, J., Pathier, E., & Bouchon, M. (2019). Evidence of su-  
821 pershear during the 2018 magnitude 7.5 Palu earthquake from space geodesy.  
822 *Nat. Geosci.*, *12*(3), 192–199. Retrieved from [http://dx.doi.org/10.1038/](http://dx.doi.org/10.1038/s41561-018-0296-0)  
823 [s41561-018-0296-0](http://dx.doi.org/10.1038/s41561-018-0296-0)<http://www.nature.com/articles/s41561-018-0296-0>  
824 doi:10.1038/s41561-018-0296-0
- 825 Tadapansawut, T., Okuwaki, R., Yagi, Y., & Yamashita, S. (2021). Rupture Process of  
826 the 2020 Caribbean Earthquake Along the Oriente Transform Fault, Involving  
827 Supershear Rupture and Geometric Complexity of Fault. *Geophys. Res. Lett.*,  
828 *48*(1), 1–9. doi:10.1029/2020GL090899
- 829 Taymaz, T., Eyidogan, H., & Jackson, J. (1991). Source parameters of large  
830 earthquakes in the East Anatolian Fault Zone (Turkey). *Geophys. J. Int.*,  
831 *106*(3), 537–550. Retrieved from [https://academic.oup.com/gji/article-](https://academic.oup.com/gji/article-lookup/doi/10.1111/j.1365-246X.1991.tb06328.x)  
832 [lookup/doi/10.1111/j.1365-246X.1991.tb06328.x](https://academic.oup.com/gji/article-lookup/doi/10.1111/j.1365-246X.1991.tb06328.x) doi:10.1111/j.1365-  
833 246X.1991.tb06328.x
- 834 Taymaz, T., Ganas, A., Yolsal-Çevikbilen, S., Vera, F., Eken, T., Erman, C., ... Öcalan,  
835 T. (2021). Source Mechanism and Rupture Process of the 24 January  
836 2020 Mw 6.7 Doğanyol–Sivrice Earthquake obtained from Seismological  
837 Waveform Analysis and Space Geodetic Observations on the East Anato-  
838 lian Fault Zone (Turkey). *Tectonophysics*, *804*(January), 228745. Retrieved  
839 from <https://linkinghub.elsevier.com/retrieve/pii/S0040195121000299>  
840 doi:10.1016/j.tecto.2021.228745
- 841 Taymaz, T., Jackson, J., & McKenzie, D. (1991). Active tectonics of the north  
842 and central Aegean Sea. *Geophys. J. Int.*, *106*(2), 433–490. Retrieved from  
843 [https://academic.oup.com/gji/article-lookup/doi/10.1111/j.1365-246X.1991](https://academic.oup.com/gji/article-lookup/doi/10.1111/j.1365-246X.1991.tb03906.x)  
844 [.tb03906.x](https://academic.oup.com/gji/article-lookup/doi/10.1111/j.1365-246X.1991.tb03906.x) doi:10.1111/j.1365-246X.1991.tb03906.x
- 845 Taymaz, T., Westaway, R., & Reilinger, R. (2004). Active faulting and crustal  
846 deformation in the Eastern Mediterranean region. *Tectonophysics*, *391*(1-  
847 4), 1–9. Retrieved from <https://linkinghub.elsevier.com/retrieve/pii/>

- 848 S0040195104002173 doi:10.1016/j.tecto.2004.07.005
- 849 ten Brink, U., Wei, Y., Fan, W., Granja-Bruña, J.-L., & Miller, N. (2020). Mysterious  
850 tsunami in the Caribbean Sea following the 2010 Haiti earthquake possibly  
851 generated by dynamically triggered early aftershocks. *Earth Planet. Sci. Lett.*,  
852 540, 116269. Retrieved from [https://linkinghub.elsevier.com/retrieve/pii/](https://linkinghub.elsevier.com/retrieve/pii/S0012821X20302120)  
853 S0012821X20302120 doi:10.1016/j.epsl.2020.116269
- 854 Toda, S., Stein, R. S., Richards-Dinger, K., & Bozkurt, S. B. (2005). Forecast-  
855 ing the evolution of seismicity in southern California: Animations built  
856 on earthquake stress transfer. *J. Geophys. Res. Solid Earth*, 110(5), 1–17.  
857 doi:10.1029/2004JB003415
- 858 Trugman, D. T., & Dunham, E. M. (2014). A 2D Pseudodynamic Rupture Model  
859 Generator for Earthquakes on Geometrically Complex Faults. *Bull. Seis-  
860 mol. Soc. Am.*, 104(1), 95–112. Retrieved from [https://doi.org/10.1785/](https://doi.org/10.1785/0120130138)  
861 0120130138[https://pubs.geoscienceworld.org/bssa/article/104/1/95-112/](https://pubs.geoscienceworld.org/bssa/article/104/1/95-112/332165)  
862 332165 doi:10.1785/0120130138
- 863 Vallée, M., Xie, Y., Grandin, R., Villegas-Lanza, J. C., Nocquet, J. M., Vaca, S.,  
864 ... Rolandone, F. (2023). Self-reactivated rupture during the 2019  
865 Mw=8 northern Peru intraslab earthquake. *Earth Planet. Sci. Lett.*, 601,  
866 117886. Retrieved from <https://doi.org/10.1016/j.epsl.2022.117886>  
867 doi:10.1016/j.epsl.2022.117886
- 868 Wang, J., Xu, C., Freymueller, J. T., Wen, Y., & Xiao, Z. (2021). AutoCoulomb:  
869 An automated configurable program to calculate coulomb stress changes on  
870 receiver faults with any orientation and its application to the 2020 Mw7.8  
871 Simeonof Island, Alaska, Earthquake. *Seismol. Res. Lett.*, 92(4), 2591–2609.  
872 doi:10.1785/0220200283
- 873 Wei, S., Fielding, E., Leprince, S., Sladen, A., Avouac, J.-P., Helmberger, D., ...  
874 Briggs, R. (2011). Superficial simplicity of the 2010 El Mayor–Cucapah  
875 earthquake of Baja California in Mexico. *Nat. Geosci.*, 4(9), 615–618. Retrieved  
876 from <http://www.nature.com/articles/ngeo1213> doi:10.1038/ngeo1213
- 877 Weiss, J. R., Walters, R. J., Morishita, Y., Wright, T. J., Lazecky, M., Wang, H., ...  
878 Parsons, B. (2020). High-Resolution Surface Velocities and Strain for Ana-  
879 tolia From Sentinel-1 InSAR and GNSS Data. *Geophys. Res. Lett.*, 47(17).  
880 Retrieved from <https://onlinelibrary.wiley.com/doi/10.1029/2020GL087376>  
881 doi:10.1029/2020GL087376
- 882 Wessel, P., & Luis, J. F. (2017). The GMT/MATLAB Toolbox. *Geochemistry, Geophys.*  
883 *Geosystems*, 18(2), 811–823. doi:10.1002/2016GC006723
- 884 Xu, S., Fukuyama, E., Ben-Zion, Y., & Ampuero, J.-P. (2015). Dynamic rup-  
885 ture activation of backthrust fault branching. *Tectonophysics*, 644–645,  
886 161–183. Retrieved from [http://dx.doi.org/10.1016/j.tecto.2015.01](http://dx.doi.org/10.1016/j.tecto.2015.01.011)  
887 .011<https://linkinghub.elsevier.com/retrieve/pii/S0040195115000554>  
888 doi:10.1016/j.tecto.2015.01.011
- 889 Xu, Y., Koper, K. D., Sufri, O., Zhu, L., & Hutko, A. R. (2009). Rupture imag-  
890 ing of the Mw 7.9 12 May 2008 Wenchuan earthquake from back projection  
891 of teleseismic P waves. *Geochemistry, Geophys. Geosystems*, 10(4), Q04006.  
892 doi:10.1029/2008GC002335



- 893 Yabuki, T., & Matsu'ura, M. (1992). Geodetic data inversion using a Bayesian  
894 information criterion for spatial distribution of fault slip. *Geophys. J. Int.*,  
895 109(2), 363–375. Retrieved from <https://onlinelibrary.wiley.com/doi/abs/10.1111/j.1365-246X.1992.tb00102.x>  
896 [https://academic.oup.com/gji/](https://academic.oup.com/gji/article-lookup/doi/10.1111/j.1365-246X.1992.tb00102.x)  
897 [article-lookup/doi/10.1111/j.1365-246X.1992.tb00102.x](https://academic.oup.com/gji/article-lookup/doi/10.1111/j.1365-246X.1992.tb00102.x) doi:10.1111/j.1365-  
898 246X.1992.tb00102.x
- 899 Yagi, Y., & Fukahata, Y. (2011). Introduction of uncertainty of Green's function into  
900 waveform inversion for seismic source processes. *Geophys. J. Int.*, 186(2), 711–  
901 720. doi:10.1111/j.1365-246X.2011.05043.x
- 902 Yagi, Y., Okuwaki, R., Enescu, B., & Lu, J. (2023). Irregular rupture process of the  
903 2022 Taitung, Taiwan, earthquake sequence. *Sci. Rep.*, 13(1), 1107. Retrieved  
904 from <https://doi.org/10.1038/s41598-023-27384-y>  
905 [https://www.nature.com/](https://www.nature.com/articles/s41598-023-27384-y)  
906 [articles/s41598-023-27384-y](https://www.nature.com/articles/s41598-023-27384-y) doi:10.1038/s41598-023-27384-y
- 907 Yamashita, S., Yagi, Y., & Okuwaki, R. (2022). Irregular rupture propagation and  
908 geometric fault complexities during the 2010 Mw 7.2 El Mayor-Cucapah  
909 earthquake. *Sci. Rep.*, 12(1), 4575. Retrieved from [https://doi.org/10.1038/](https://doi.org/10.1038/s41598-022-08671-6)  
910 [s41598-022-08671-6](https://www.nature.com/articles/s41598-022-08671-6)  
911 <https://www.nature.com/articles/s41598-022-08671-6>  
912 doi:10.1038/s41598-022-08671-6
- 911 Yamashita, S., Yagi, Y., Okuwaki, R., Shimizu, K., Agata, R., & Fukahata, Y. (2022).  
912 Potency density tensor inversion of complex body waveforms with time-  
913 adaptive smoothing constraint. *Geophys. J. Int.*, 231(1), 91–107. Re-  
914 trieved from <https://academic.oup.com/gji/article/231/1/91/6584392>  
915 doi:10.1093/gji/ggac181
- 916 Yao, H., Gerstoft, P., Shearer, P. M., & Mecklenbräuker, C. (2011). Compressive  
917 sensing of the Tohoku-Oki Mw 9.0 earthquake: Frequency-dependent rupture  
918 modes. *Geophys. Res. Lett.*, 38(20). doi:10.1029/2011GL049223
- 919 Yıkılmaz, M. B., Turcotte, D. L., Heien, E. M., Kellogg, L. H., & Rundle, J. B.  
920 (2015). Critical Jump Distance for Propagating Earthquake Ruptures  
921 Across Step-Overs. *Pure Appl. Geophys.*, 172(8), 2195–2201. Retrieved from  
922 <http://link.springer.com/10.1007/s00024-014-0786-y> doi:10.1007/s00024-  
923 014-0786-y
- 924 Zahradník, J., Turhan, F., Sokos, E., & Gallovič, F. (2023). List of authors This is  
925 a non - peer reviewed preprint submitted to EarthArXiv. *EarthArXiv*, 1–20.  
926 doi:10.31223/X5T666

Supporting Information for

# **Multi-scale rupture growth with alternating directions in a complex fault network during the 2023 south-eastern Türkiye and Syria earthquake doublet**

**Ryo Okuwaki<sup>1</sup>, Yuji Yagi<sup>1</sup>, Tuncay Taymaz<sup>2</sup>, Stephen P. Hicks<sup>3</sup>**

<sup>1</sup>Faculty of Life and Environmental Sciences, University of Tsukuba, Tsukuba, Ibaraki 305-8572, Japan

<sup>2</sup>Department of Geophysical Engineering, The Faculty of Mines, Istanbul Technical University, Maslak, 34469  
Sariyer, Istanbul, Türkiye

<sup>3</sup>Department of Earth Sciences, University College London, Gower Street, London, WC1E 6BT, UK

## **Contents**

- Tables S1 and S2
- Figures S1–S11
- Movies S1–S3 (captions)

---

Corresponding author: Ryo Okuwaki, [rokuwaki@geol.tsukuba.ac.jp](mailto:rokuwaki@geol.tsukuba.ac.jp)

**Table S1.** Near-source structure used for calculating Green's functions, adopted from CRUST1.0 model (Laske et al., 2013).

$V_P$ (km/s)	$V_S$ (km/s)	Density (g/cm <sup>3</sup> )	Thickness (km)
6.00	3.52	2.72	17.64
6.30	3.68	2.79	8.90
6.60	3.82	2.85	9.64
8.08	4.49	3.33	- (below moho)

**Table S2.** An alternative near-source structure used for calculating Green's functions, adopted from ak135 model (Kennett et al., 1995).

$V_P$ (km/s)	$V_S$ (km/s)	Density (g/cm <sup>3</sup> )	Thickness (km)
5.80	3.46	2.45	20.0
6.50	3.85	2.71	15.0
8.04	4.48	3.30	- (below moho)

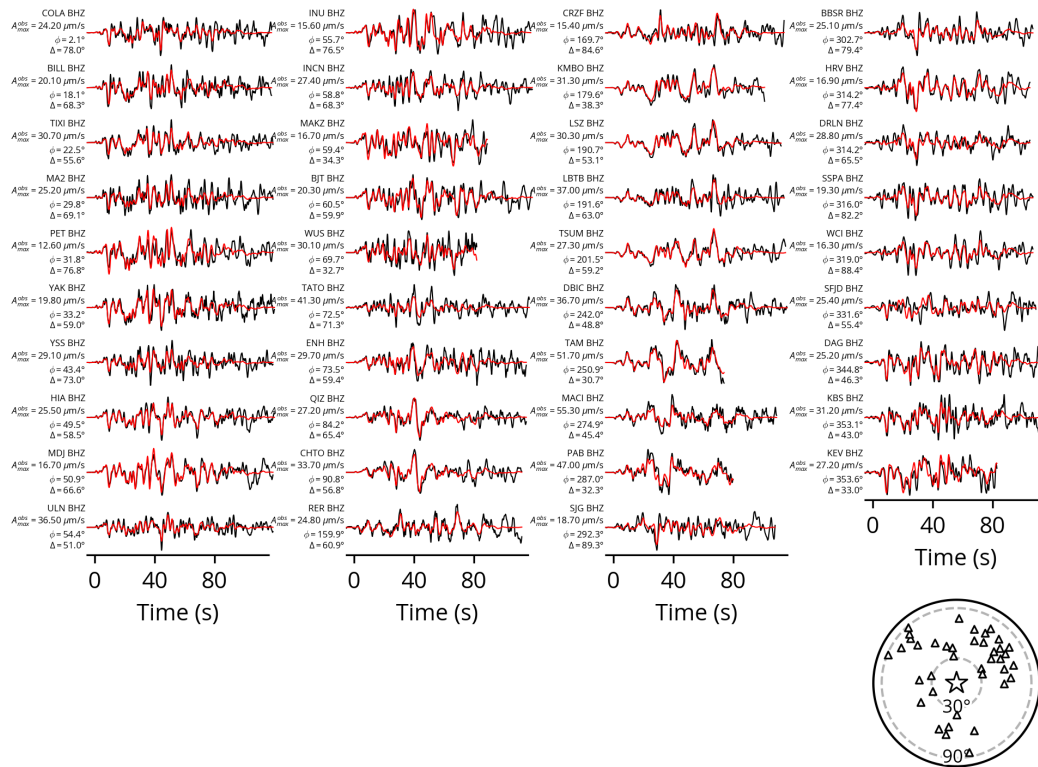


**Figure S1.** Waveform fits of the initial  $M_W$  7.9 earthquake model. The black and red traces are the observed and synthetic waveforms. The station code and channel, the maximum amplitude of observed waveform ( $A_{\max}^{\text{obs}}$ ), the station azimuth ( $\phi$ ), and the epicentral distance ( $\Delta$ ) are shown on the left of each panel. The bottom map is an azimuthal equidistant projection of the station distribution (triangle). The star shows the epicenter. The dashed lines are the epicentral distances at  $30^\circ$  and  $90^\circ$ .

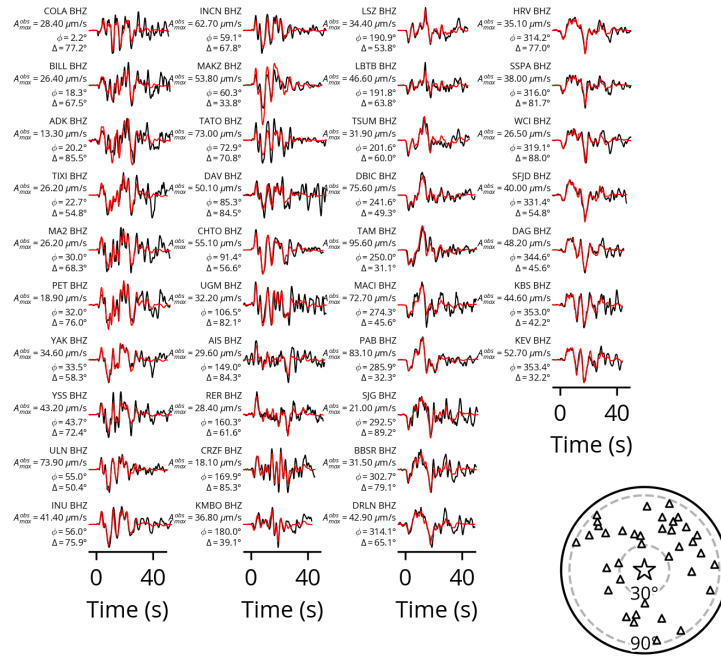


**Figure S2.** Waveform fits of the secondary  $M_W$  7.6 earthquake model. The black and red traces are the observed and synthetic waveforms. The station code and channel, the maximum amplitude of observed waveform ( $A_{\max}^{\text{obs}}$ ), the station azimuth ( $\phi$ ), and the epicentral distance ( $\Delta$ ) are shown on the left of each panel. The bottom map is an azimuthal equidistant projection of the station distribution (triangle). The star shows the epicenter. The dashed lines are the epicentral distances at  $30^\circ$  and  $90^\circ$ .

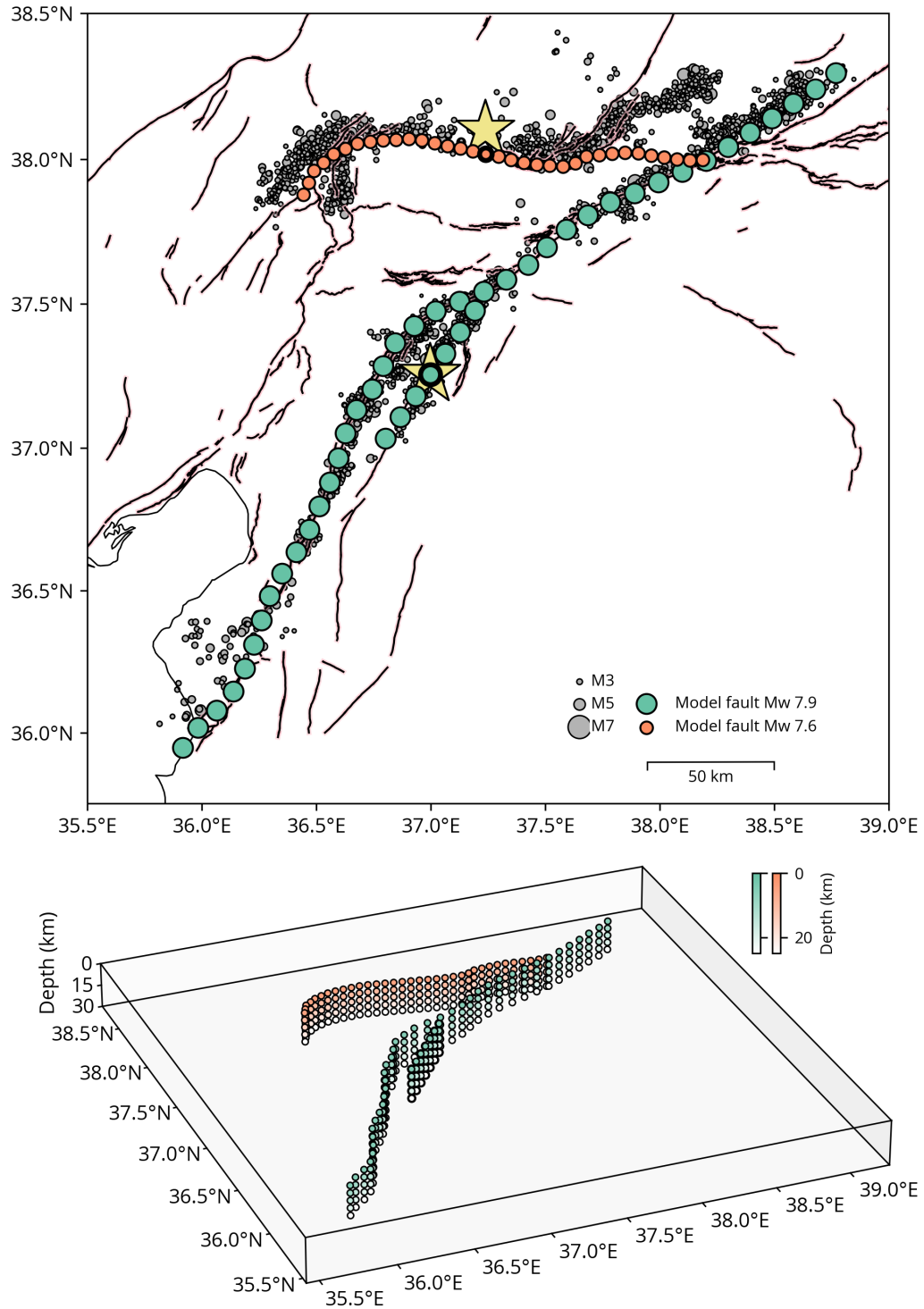


**Figure S3.** Model-fault geometries for the  $M_W$  7.9 (green) and  $M_W$  7.6 (orange) earthquakes used for our potency-density tensor inversion. The colored dots shows the location of the source elements. The hypothesized initial rupture point is marked as a thick black circle on a map. The relocated mainshocks (stars), aftershocks (gray dots), and active faults are the same as shown in Fig. 1.

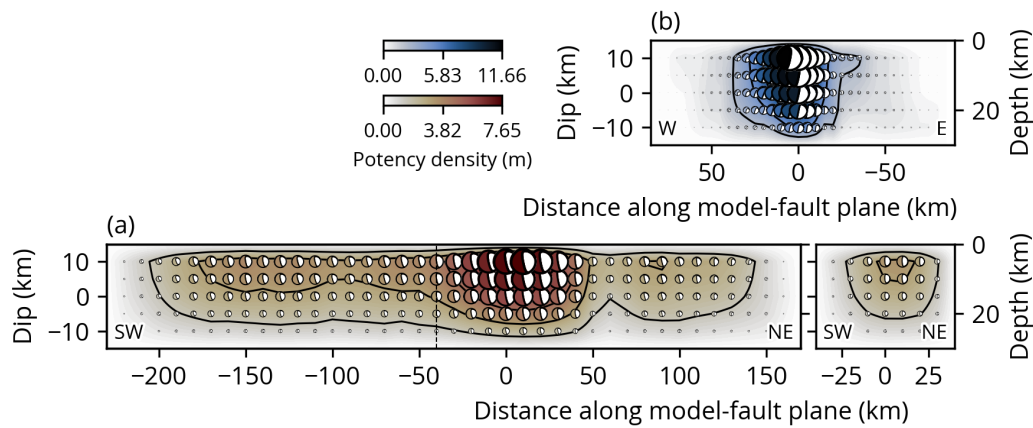


**Figure S4.** Cross sections of the total potency-density tensor distributions for (a) the  $M_W$  7.9 (reddish) and (b) the  $M_W$  7.6 (blueish) earthquakes. The beachball is the lower hemisphere projection of the moment tensor drawn by using Pyrocko (Heimann et al., 2017), which is projected on a plane of {strike, dip} = { $54^\circ$ ,  $90^\circ$ } for the panels (a) and {strike, dip} = { $278^\circ$ ,  $90^\circ$ } for the panel (b). The size of the beachball is scaled by potency density. The abscissa is a distance from the hypothesized initial rupture point along the non-planar model fault. For each panel, the vertical axis (Y-axis) is stretched by a factor of 2 for the visibility of the figure. The dashed line on panel (a) denotes the point on the EAF, which is closest to the initial rupture point on the splay model fault. The panel (b) is flipped horizontally so that it can intuitively be compared with map view of the corresponding model ( $M_W$  7.6 earthquake) in Fig. 2. The black contours are drawn at every 1.5 m (lower panels) and 2.3 m (upper panel) for the  $M_W$  7.9 and the  $M_W$  7.6 earthquakes, respectively.

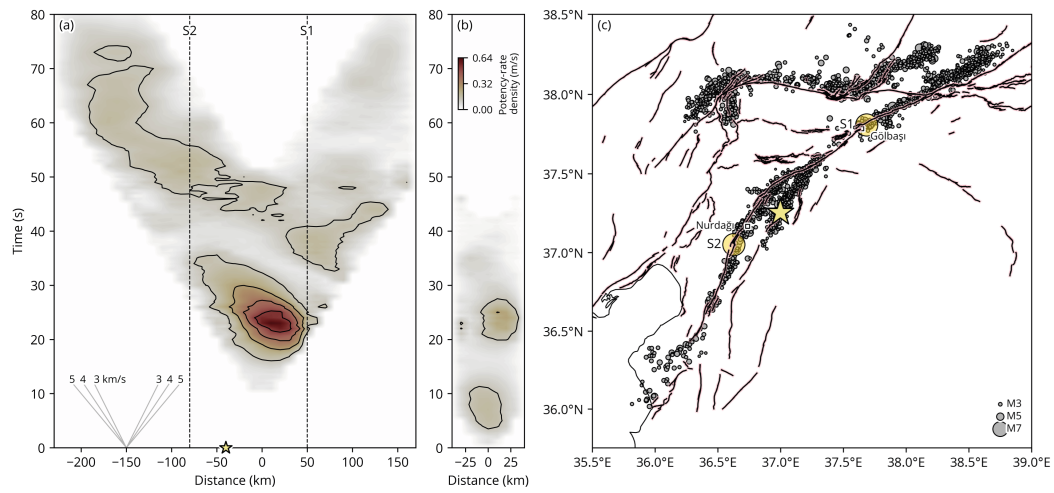


**Figure S5.** Comparison between (a) the potency-rate density tensor distribution and (b) the active faults. The dashed lines indicate the approximate positions of the steps, shown on a map (c) as S1 and S2. Panels (a,b) are from Fig. 2, and the active faults, the mainshocks, and the aftershocks are the same as shown in Fig. 1.

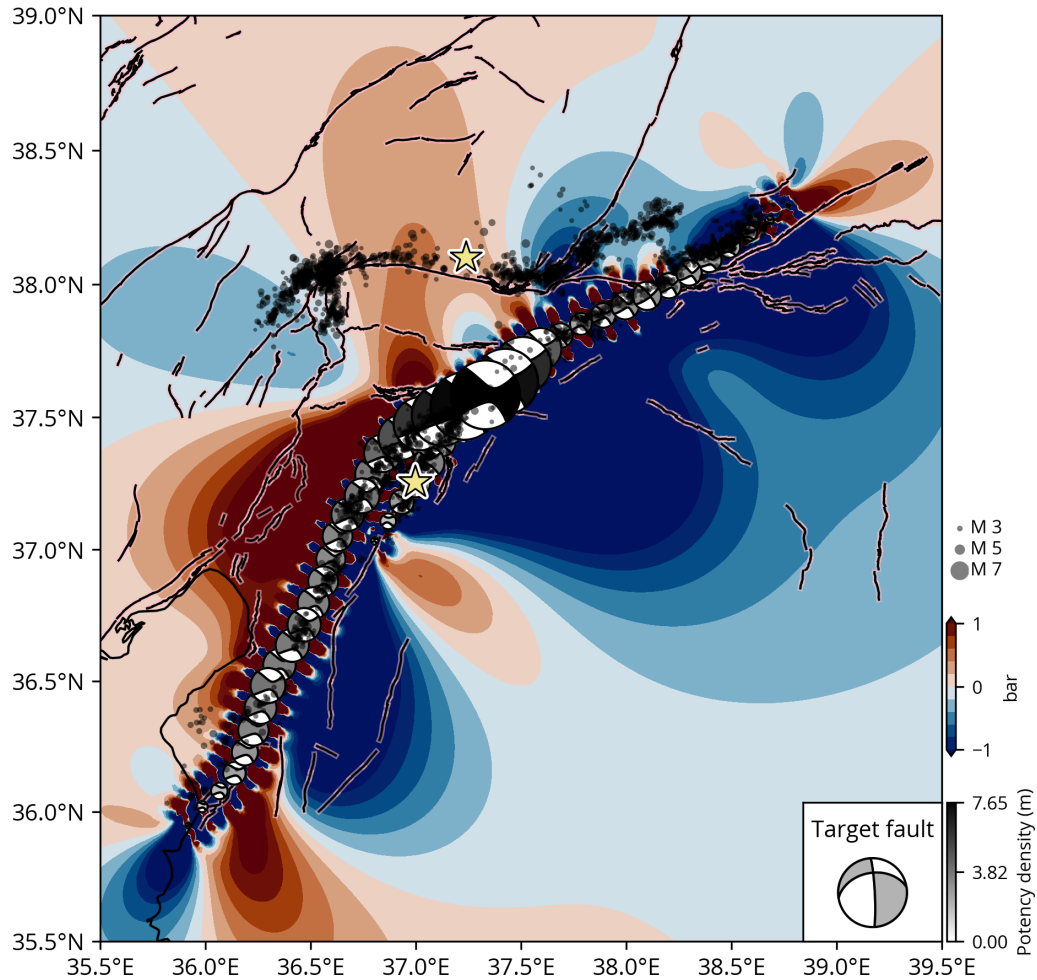


**Figure S6.** The Coulomb stress change (King et al., 1994; Lin & Stein, 2004; Toda et al., 2005; Wang et al., 2021) from our preferred solution (Fig. S4a) to the target fault of the  $M_W$  7.6 earthquake (inset), averaged over 5–30 km depths. The Coulomb stresses are calculated with a friction coefficient of 0.4, poisson ratio of 0.25, and Young’s modulus of  $8 \times 10^5$  bars. The target fault is of  $261^\circ/42^\circ/-8^\circ$  (strike/dip/rake) from the GCMT solution for the  $M_W$  7.6 earthquake (Dziewonski et al., 1981; Ekström et al., 2012). The relocated mainshocks (stars), aftershocks (gray dots), and active faults are the same as shown in Fig. 1.



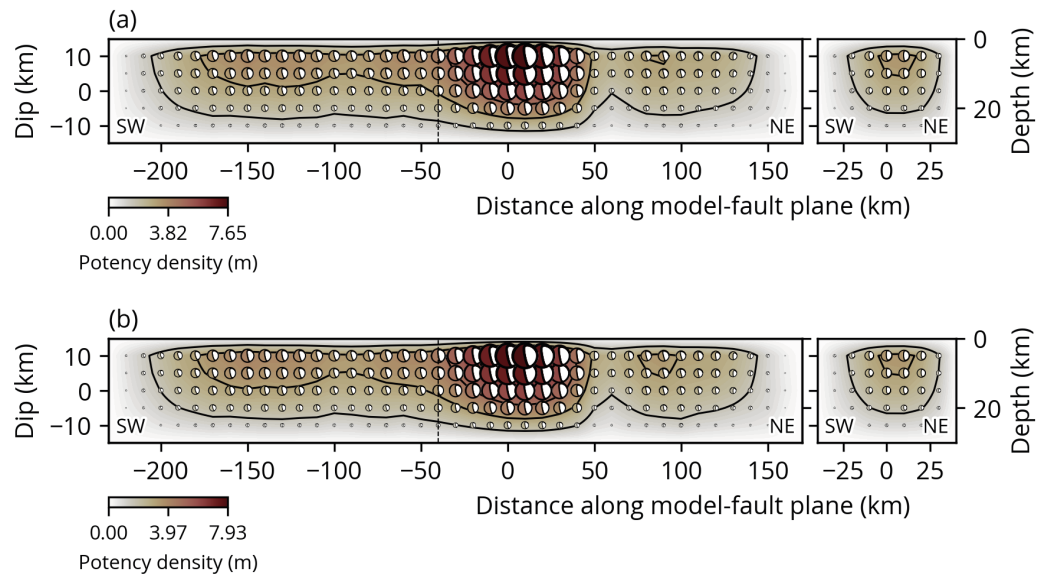


**Figure S7.** Comparison of solutions using different velocity structure models adopted from (a) the CRUST1.0 model (Laske et al., 2013) (Table S1) and (b) the ak135 model (Kennett et al., 1995) (Table S2). The beachball shows the lower-hemisphere projection of the moment tensor calculated by integrating the potency-rate density tensors with respect to time at each source element with its size scaled with the potency, which is projected on a plane of {strike, dip} = {54°, 90°}

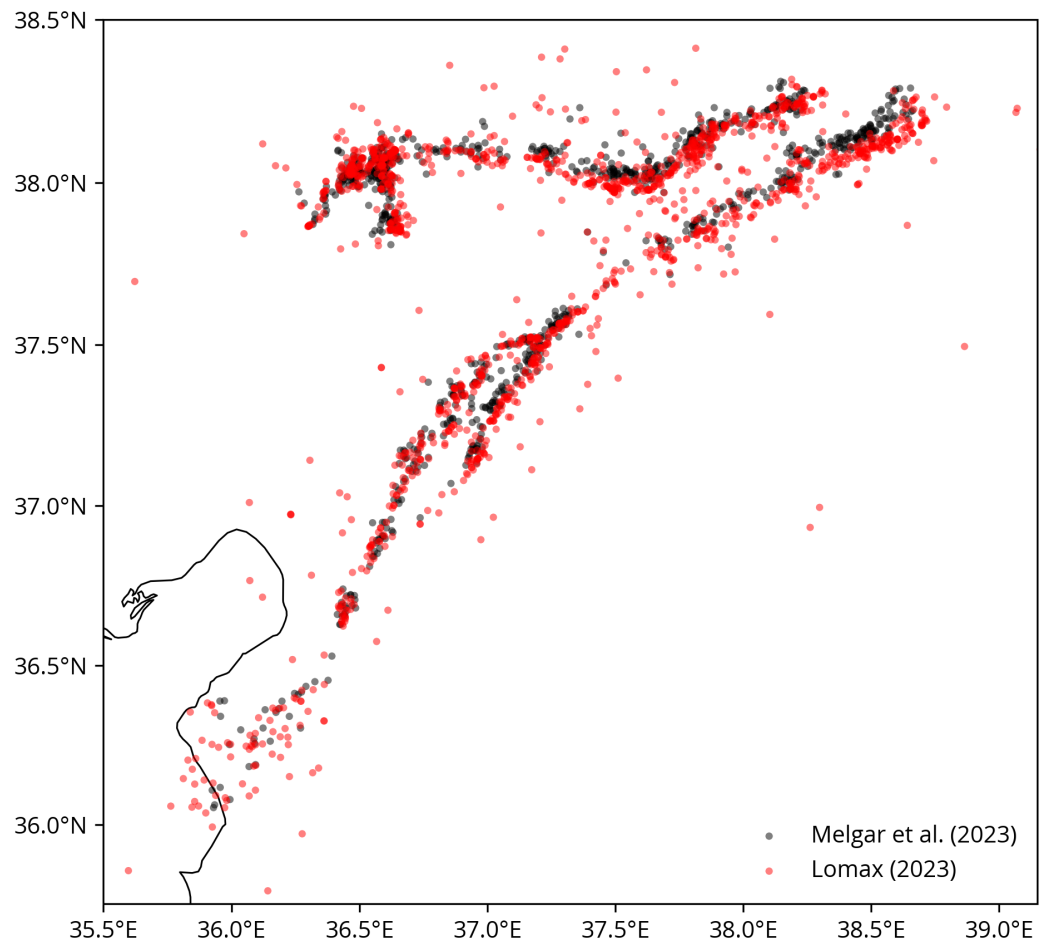


**Figure S8.** Comparison of aftershock distributions from Melgar et al. (2023) and Lomax (2023) (magnitude>3; from 2023-02-06 to 2023-02-13)

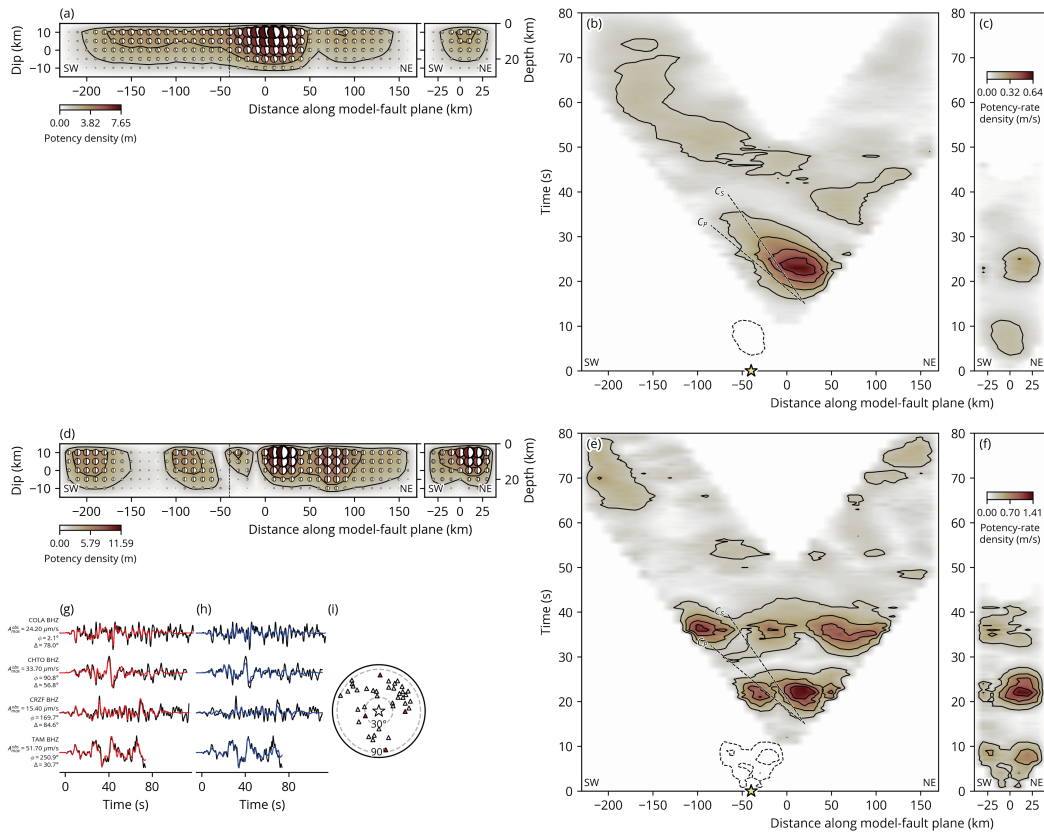


**Figure S9.** Comparison of solutions using different bases tensor constraints. The panels (a–c) show our preferred solution, and the panels (d–f) show the solution by constraining the potency to be only strike-slip. Specifically, this constraint is realized by adopting only two components of basis moment tensors of M1 and M2 designed by Kikuchi and Kanamori (1991) (see Figure 1 in Kikuchi and Kanamori (1991)). The selected waveform fits from (g) our preferred solution and (h) the restricted solution. The black trace is the observed waveform and the colored trace is the synthetic waveform. The panel (i) is the station distribution, where the stations displayed in the panels (g) and (h) are highlighted by red. All the other symbols and the ways of projection presented in this figure are the same as shown in Figs. 2 and S4.

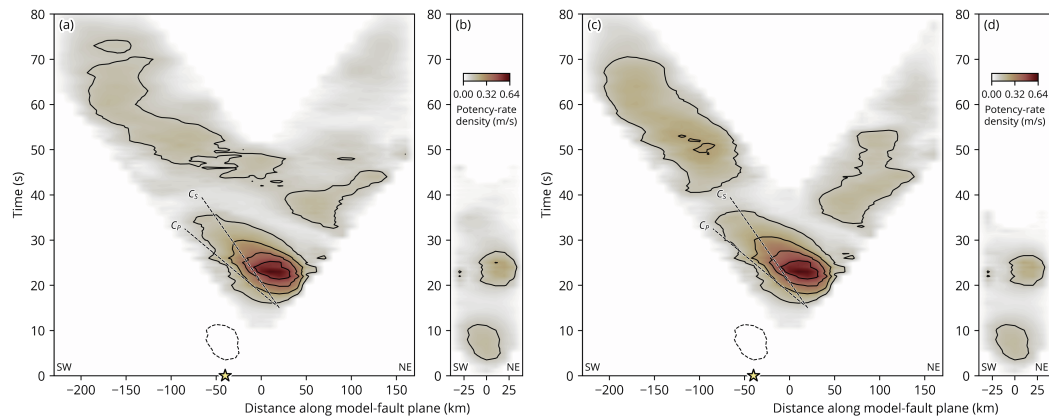


**Figure S10.** Comparison of solutions using different assumptions of maximum duration of potency-rate density functions. The panel (a,b) shows our preferred solution assuming a 42-s duration, and the panel (c,d) shows the alternative solution assuming a 32-s duration. The symbols and projection are the same as those of Figure 2.

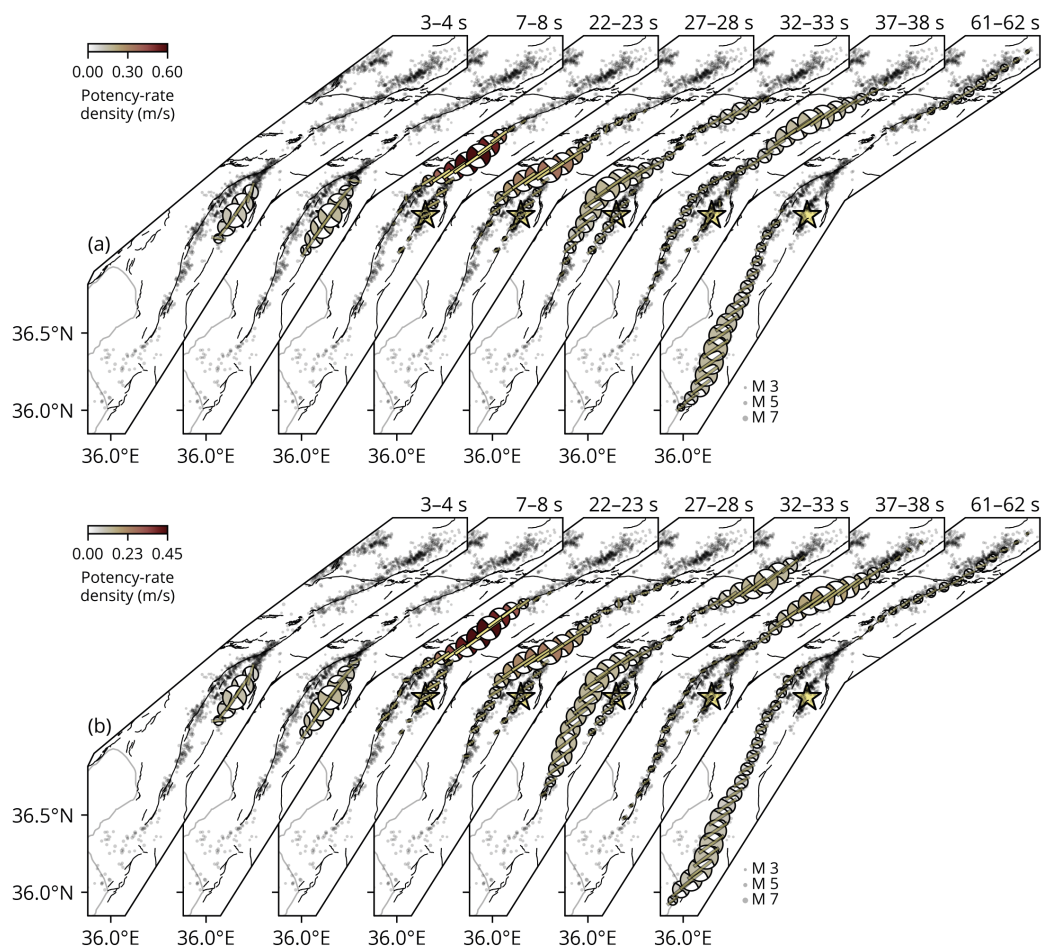


**Figure S11.** Comparison of solutions using different assumptions of hypothesized rupture-front velocity at (a) 4 km/s and (b) 5 km/s. The symbols and projection are the same as those of Figure 3.

**Movie S1.** Cross sections of the spatiotemporal potency-rate density tensor distribution for (a,b) the  $M_W$  7.9 earthquake and (c) the  $M_W$  7.6 earthquake. Panel (b) is the splay fault domain. The X-axis is the distance along the non-planar model-fault plane. The “0” on the X-axis means our hypothesized initial rupture point, except for Panel (a), which corresponds to the location of junction between the splay fault and the main EAF. The dashed line on Panel (a) denotes the point on the EAF, which is closest to the initial rupture point on the splay model fault. Note that Panel (c) is flipped horizontally so the right-hand side is orienting to east.

**Movie S2.** Map view of the spatiotemporal potency-rate density tensor distribution for the  $M_W$  7.9 earthquake. The size of the beachball is scaled by the maximum potency-rate density for each model. The moment-rate function (left top) and the temporal evolution of the potency-rate density distribution (right top) are the same as shown in Fig. 2. The epicenters (stars), aftershocks, and active faults are the same as shown in Fig. 1.

**Movie S3.** Same as Movie S2, but for the  $M_W$  7.6 earthquake.

## References in the Supporting Information

- Dziewonski, A. M., Chou, T.-A., & Woodhouse, J. H. (1981). Determination of earthquake source parameters from waveform data for studies of global and regional seismicity. *J. Geophys. Res. Solid Earth*, 86(B4), 2825–2852. doi:10.1029/JB086iB04p02825
- Ekström, G., Nettles, M., & Dziewoński, A. (2012). The global CMT project 2004–2010: Centroid-moment tensors for 13,017 earthquakes. *Phys. Earth Planet. Inter.*, 200–201, 1–9. doi:10.1016/j.pepi.2012.04.002
- Heimann, S., Kriegerowski, M., Isken, M., Cesca, S., Daout, S., Grigoli, F., ... Vasyura-Bathke, H. (2017). *Pyrocko - An open-source seismology toolbox and library*. GFZ Data Services. doi:10.5880/GFZ.2.1.2017.001
- Kennett, B. L., Engdahl, E. R., & Buland, R. (1995). Constraints on seismic velocities in the Earth from traveltimes. *Geophys. J. Int.*, 122(1), 108–124. doi:10.1111/j.1365-246X.1995.tb03540.x
- Kikuchi, M., & Kanamori, H. (1991). Inversion of complex body waves-III. *Bull. Seism. Soc. Am.*, 81(6), 2335–2350. doi:10.1785/BSSA0810062335
- King, G. C., Stein, R. S., & Lin, J. (1994). Static stress changes and the triggering of earthquakes. *Bull. Seismol. Soc. Am.*, 84(3), 935–953. doi:10.1785/BSSA0840030935
- Laske, G., Masters, T. G., Ma, Z., & Pasyanos, M. (2013). Update on CRUST1.0 - A 1-degree Global Model of Earth's Crust. *Geophys. Res. Abstr.* 15, *Abstr. EGU2013-2658*, 15, Abstract EGU2013–2658. (<https://igppweb.ucsd.edu/~gabi/crust1.html>)
- Lin, J., & Stein, R. S. (2004). Stress triggering in thrust and subduction earthquakes and stress interaction between the southern San Andreas and nearby thrust and strike-slip faults. *J. Geophys. Res. Solid Earth*, 109(B2), 1–19. doi:10.1029/2003jb002607
- Lomax, A. (2023). *Precise, NLL-SSST-coherence hypocenter catalog for the 2023 Mw 7.8 and Mw 7.6 SE Turkey earthquake sequence*. Zenodo. Retrieved from <https://doi>

- .org/10.5281/zenodo.7727678 doi:10.5281/zenodo.7727678
- Melgar, D., Taymaz, T., Ganas, A., Crowell, B., Öcalan, T., Kahraman, M., ... Altuntaş, C. (2023). Sub- and super-shear ruptures during the 2023 Mw 7.8 and Mw 7.6 earthquake doublet in SE Türkiye. *Seismica*, 2(3), 1–14. doi:10.26443/seismica.v2i3.387
- Toda, S., Stein, R. S., Richards-Dinger, K., & Bozkurt, S. B. (2005). Forecasting the evolution of seismicity in southern California: Animations built on earthquake stress transfer. *J. Geophys. Res. Solid Earth*, 110(5), 1–17. doi:10.1029/2004JB003415
- Wang, J., Xu, C., Freymueller, J. T., Wen, Y., & Xiao, Z. (2021). AutoCoulomb: An automated configurable program to calculate coulomb stress changes on receiver faults with any orientation and its application to the 2020 Mw7.8 Simeonof Island, Alaska, Earthquake. *Seismol. Res. Lett.*, 92(4), 2591–2609. doi:10.1785/0220200283